

Unclassified

SECURITY CLASSIFICATION OF THIS PAGE

Form Approved
OMB No. 0704-0188

REPORT DOCUMENTATION PAGE

1a. REPORT SECURITY CLASSIFICATION

Unclassified

2a. SECURITY CLASSIFICATION AUTHORITY

DTIC
SELECTED
MAR 30 1995
G

1b. RESTRICTIVE MARKINGS

3. DISTRIBUTION/AVAILABILITY OF REPORT

Approved for public release;
Distribution unlimited

4. PERFORMING ORGANIZATION REPORT NUMBER(S)

5. MONITORING ORGANIZATION REPORT NUMBER(S)

AFOSR-TR-95-0175

6a. NAME OF PERFORMING ORGANIZATION

6b. OFFICE SYMBOL
(If applicable)

7a. NAME OF MONITORING ORGANIZATION

University of Oslo

Air Force Office of Scientific Research

6c. ADDRESS (City, State, and ZIP Code)

Faculty of Science, PO Box 1032 Blindern
N-0316 OSLO, NORWAY

7b. ADDRESS (City, State, and ZIP Code)

Building 410
Bolling AFB D C 20332-6448

8a. NAME OF FUNDING/SPONSORING ORGANIZATION

8b. OFFICE SYMBOL
(If applicable)

9. PROCUREMENT INSTRUMENT IDENTIFICATION NUMBER

AFOSR

NL

F49620-92-J-0510

10. SOURCE OF FUNDING NUMBERS

PROGRAM ELEMENT NO.	PROJECT NO.	TASK NO.	WORK UNIT ACCESSION NO.
100000	AFOSR	104	

11. TITLE (Include Security Classification)

Eurasian Seismic Surveillance - 2D FD Seismic Synthetics and
Event Discrimination

12. PERSONAL AUTHOR(S)

Bent O. Ruud, Eystein S. Husebye

13a. TYPE OF REPORT

Final Technical Report

13b. TIME COVERED

FROM 1 Oct 92 TO 30 Sep 94

14. DATE OF REPORT (Year, Month, Day)

1995 February 23

15. PAGE COUNT

16. SUPPLEMENTARY NOTATION

17. COSATI CODES

FIELD	GROUP	SUB-GROUP

18. SUBJECT TERMS (Continue on reverse if necessary and identify by block number)

2D FD synthetics including topography, inversion for crustal
structure, real-time magnitude estimation, seismic event
classification

19. ABSTRACT (Continue on reverse if necessary and identify by block number)

Most efforts have been devoted to 2D FD synthetics for simulating seismic wave propagation in a complex lithosphere. The FD scheme used is tied to the numerical solution of the elastodynamic wave equation. We have demonstrated the usefulness of this approach by computing synthetic seismograms for a set of progressively complex lithosphere models. In practice, model set-up for FD computations have proved cumbersome so we have elaborated on automating structural model generation. The computed synthetics are SEG-Y formatted and thus are easily processed using standard software packages like the ProMAX.

As part of the 2D FD studies, we have critically examined optimal design of boundary conditions in order to reduce edge reflection artefacts. Our synthetic wavefield scheme recently extended to 3D modelling can also handle surface topography
(continues on next page)

20. DISTRIBUTION/AVAILABILITY OF ABSTRACT

UNCLASSIFIED/UNLIMITED SAME AS RPT. DTIC USERS

21. ABSTRACT SECURITY CLASSIFICATION

Unclassified

22a. NAME OF RESPONSIBLE INDIVIDUAL

22b. TELEPHONE (Include Area Code)

(202) 767-4964

22c. OFFICE SYMBOL

AFOSR/NL

19950328104

In the latter case, we have been able to simulate in 3D Rg-scattering observations as observed at the NORESS array. Crustal wave propagation is important in a monitoring context so we have studied in a realistic manner the relevance of overly detailed crustal models frequently published in the scientific litteratur. These experiments were tied to synthetic wavefields generated both for homogeneous and inhomogeneous (3 percent perturbation), and then trying to recover the original models through tau-p related analysis and inversion. Even for oversimplified homogeneous crustal models (no P- and S-coda excitation) we were not able to recover the original crustal model in detail. We concluded that a crust with linearized velocity increases in combination with 2 - 4 percent velocity pertubations is a better approximation to real Earth structures than the often published, homogeneous multilayered models.

Event magnitude is an versatile parameter in many seismological studies not at least in the context of nuclear test ban monitoring. For simulating network signal detection capabilities the noise level at individual stations are needed in near real time which in practice appears to be difficult to obtain. Ideally, we would prefer to have such noise level estimates available on-line to measure the 'on-line threshold monitoring' performance and likewise event magnitudes. To achieve this we have been exploring the usefulness of a random vibration theory

Contents

1 Objectives	3
2 Report summary	3
2.1 Outline of the report	5
3 3D FD modeling of scattering from topographic relief	7
3.1 Results and discussion	8
3.2 Concluding remarks	11
4 Appendix A	A1-A6
5 Appendix B	B1-B13
6 Appendix C	C1-C12
7 Appendix D	D1-D18

Accession For	
NTIS	CRA&I
DTIC	TAB
Unannounced	<input type="checkbox"/>
Justification _____	
By _____	
Distribution / _____	
Availability Codes	
Dist	Avail and / or Special
A-1	

List of publications supported by this contract

First Scientific Report (19. May, 1993)

Hestholm, S.O., Husebye, E.S. and Ruud, B.O., 1994. Seismic wave propagation in complex crust – upper mantle media using 2D finite difference synthetics, *Geophys. J. Int.*, 118, 643-670.

First Annual Technical Report (22. Dec., 1993)

Tarvainen, M. and Husebye, E.S., 1994. Spatial and temporal patterns of the Fennoscandian seismicity – an exercise in explosion monitoring, *Geophysica*, 29, 1-19.

Hestholm, S.O. and Ruud, B.O., 1994. 2D finite difference elastic wave modeling including surface topography, *Geophysical Prospecting*, 42, 371-390.

Final Technical Report (this report)

Mendi, C.D. and Husebye, E.S., 1994. Near real time seismic magnitude and moment measurements, *Annali di Geofisica*, 37, 365-382.

Ruud, B.O., Grundt, Y., and Husebye, E.S., 1995. A comparison of tau-sum velocity-depth inversion for a perturbed and unperturbed model, m/s prepared for publication.

Simone, A. and Hestholm, S., 1995. Optimal absorbing boundary condition in 2D finite difference elastic wave modeling. Empirical study and comparison with exponential damping, m/s prepared for publication.

Hestholm, S.O. and Ruud, B.O., 1995. 3D FD modeling of scattering from topographic relief, m/s in preparation.

Theses/Dissertations

Bent O. Ruud submitted in Oct 1994 to the University of Bergen a thesis based on research conducted under AFOSR contracts, requesting permission to defend this scientific endeavour for the degree of Doctor of Philosophy. Permission was granted and the thesis was successfully defended on 20 Jan 1995; opponents were Dr. Anton M. Dainty, Phillis Lab., Hanscom AFB, USA and Prof. David Gubbins, University of Leeds, UK.

Ph.D. students involved in contract work

Stig O. Hestholm and C. Deniz Mendi would probably submit their Ph.D. thesis for defence later this year.

Honors/Awards

In May 1994 Prof. Eystein S. Husebye was granted the equivalent of US\$ 72,000.- by NATO Scientific Affairs Division, Bruxelles, Belgium for arranging a NATO Advanced Study Institute on the theme "Monitoring a Comprehensive Test Ban Treaty". Planning for the NATO ASI took place in the Fall 1994 and the conference itself took place in Alvor, Portugal from 23 Jan to 2 Feb, 1995. Most participants rated this NATO ASI a great success and much credit for this should go to Dr. A. M. Dainty, one of the Scientific Directors.

1 Objectives

- Foster a better understanding of seismic wave propagation in complex lithospheric media.
- Principal modeling tool is 2D finite difference (FD) synthetics for models also including surface topography.
- Corroborating synthetics through analysis of array and network data.
- Use 'synthetic' knowledge in design of event classification schemes.
- Seismic network performance.

Note, a basic element in research is curiosity which in practice will imply a certain flexibility regarding adherence to objectives.

2 Report summary

Most efforts have been devoted to 2D FD synthetics for simulating seismic wave propagation in a complex lithosphere. The FD scheme used is tied to the numerical solution of the elastodynamic wave equation. Spatial partial differentiation is achieved through cost-optimized, dispersion-bounded, high-order finite difference operators on a staggered grid. For time stepping, a leap-frog technique is used. For the numerical dispersion relations, the stability limit and bandwidth introduced by the discretization, the reader is referred to Sguazzero, Kindelan and Kamel (1989).

Recently we have demonstrated the usefulness of this approach by computing synthetic seismograms for a set of progressively complex lithosphere models (Hestholm, Husebye and Ruud, 1994). In practice, model set-up for FD computations have proved cumbersome so we have elaborated on automating structural model generation. The new approach now working satisfactorily is tied to using a scanner for reading say a published multilayered crustal model. For any model point, proper layer assignment is performed automatically and hence a corresponding specification of physical parameters like velocity and density is obtained. The computed synthetics are SEG-Y formatted and thus are easily processed using standard software packages like the popular ProMAX.

The method of τ -sum inversion provide a convenient way to estimate velocity-depth models from seismic profiling data via $\tau - p$ transformation. Two basic assumptions must be valid: (i) the velocity must increase monotonically with depth, and (ii) the medium must be laterally homogeneous. In a new paper we test the sensitivity of the inversion method for small deviations from the second of these assumptions by inverting synthetic seismograms computed for two models, one laterally homogeneous and the other perturbed by a 2-dimensional random field. The synthetics were generated by finite difference modeling of the elasto-dynamic wave equation. Also the general resolution of the method for the actual frequency bandwidth (1-5 Hz) and the experimental layout (1 shot, sensors at 0.4 km intervals out to 320 km offset) could be attained. The results showed that for the perturbations used (von Kármán correlation function of order 0.3, correlation distances of 10 km and 2.5 km in the horizontal and vertical directions respectively, and an RMS of 3%) the model could be recovered with about the same accuracy whether perturbed or not. The general resolution in velocity was about 0.2 km/s all the way down to the Moho. The results were somewhat surprising in view of the rather strong scattering produced by the perturbations,

wiping out most of the phases observable for the unperturbed model. The success of the inversion method in recovering the large scale structure of the velocity-depth function is attributed to the fact that it depends only on the strongest post-critically reflected phases. However, fine scale layering of the models was unrecoverable even for the unperturbed model.

An important motivation for this particular study was a disbelief in the realism of the many finely layered crustal models derived from large-scale wide-angle reflection and refraction profiling experiments. Simply, the claimed crustal models hardly have a counterpart vis-a-vis the field observations at hand. Our disbelief in such models have been further strengthened during the experiments described here - under ideal simulated observational conditions like no background noise, dense spatial wavefield sampling and using typical crustal layer velocities - still we are unable to retrieve the finer details of the a priori known crustal model. Adding velocity perturbations, a prerequisite for generating realistic synthetics in terms of P- and S-coda excitation, crustal layering details are definitely non-retrievable. To summarize; simple crustal models in terms of linearized velocity increases with depth and in combination with structural perturbations of 2-4 per cent appear to match real Earth structures far better than elaborated, multilayered crustal models.

Event magnitude is a versatile parameter in many seismological studies not at least in the context of nuclear test ban monitoring. For simulating network signal detection capabilities the noise level at individual stations are needed in near real time which in practice appears to be difficult to obtain. Ideally, we would prefer to have such noise level estimates available on-line to measure the 'on-line threshold monitoring' performance (Ringdal and Kværna, 1989). To achieve this we have been exploring the usefulness of a random vibration theory formula, namely (Cartwright and Longnet-Higgins, 1956).

$$A_{max} = f(N)A_{rms} \quad (1)$$

where A_{max} is max amplitude; $f(N) = N(2 \ln N)^{1/2}$ where N is the number of extrema with the RMS-window and A_{rms} is amplitude root-mean-square. Most signal detections in use are of the STA/LTA type where the short-term-average (STA) is in fact a root-mean-square (RMS) trace estimate. Initial test results from real recordings indicate that the above formula is valid; error estimates amount to ± 0.1 magnitude unit. In other word, on-line magnitude estimation should be feasible. Extensive analysis of explosion and earthquake recordings by the Norwegian Seismological Network indicated that this is valid for practical seismological purposes. On this basis, we undertook local M_L (Lg) magnitude estimations for 30 events; satisfactory results were obtained as our novel M_L determinations were very similar to those reported by NORSAR (Mendi and Husebye, 1994).

Local magnitude estimation is an important issue in the seismic monitoring context, but in practise often somewhat problematic due to lack of proper empirical signal frequency-distance correction curves. To overcome this kind of problems, we constructed 'theoretical' frequency-distance curves for Scandinavia using attenuation and geometrical spreading constants as published by Sereno et al (1988). Good agreement was obtained with conventional correction curves thus demonstrating that local magnitude estimation procedures are transportable conditioned on available geometric spreading and attenuation constants.

Finally, a comprehensive study aimed at seismic event classification at local and regional distances was considered. Preparatory efforts here comprise software development and selection of a comprehensive data base; we opted for the NORESS and ARCESS events used by Lacoss et al. (1992). Regrettably, we cannot report much progress on this issue under this contract. What

we have done so far was to compute the P/Lg amplitude ratios for the 30 events analysed in the Mendi and Husebye (1994) study, also in an automated manner. The results obtained were not very positive as regards this particular discriminant as there were no clear distinction between the earthquake and explosion populations. It is probably several reasons for this; firstly, source-receiver paths are often offshore in a continental crustal regime with many thick sedimentary basins; secondly, the 'ground truth' aspect of the Bergen University bulletin is poor, as the earthquakes and explosions are frequently intermixed. Close inspection of our results indicate that the very calculations of P/Lg discriminant parameters via the A_{rms} relation given in eq.(1) would provide in near real time information bearing on the source identification.

2.1 Outline of the report

In the next section of this Final Technical Report under Contract AFOSR Grant F49620-92-5-0510 we describe the most recent research accomplished concerning modeling of scattering from topographic relief near the NORESS array. This work is performed with a new 3D elasto-dynamic finite difference code allowing for topography at the free surface. The theoretical details of this novel method is given in Appendix A. We plan to continue to work on this interesting modeling experiments under the AFOSR Grant F49620-94-1-0278 at the University of Bergen. In Appendix B we include a new paper by Simone and Hestholm (1995) concerning the absorbing boundary method used in our finite difference programs. The complete text of the Ruud et al (1995) paper of tau-p inversion of synthetic 2D FD refraction and wide-angle reflection profiles is given in Appendix C, and in Appendix D we include the already published paper by Mendi and Husebye (1994) on near real time magnitude estimation.

References

Cartwright, D.E., and Longuet-Higgins, M.S., 1956. The statistical distribution of the maxima of a random function, *Proc. Roy. Soc. London, Ser. A* **237**, 212-223.

Hestholm, S.O., Husebye, E.S., and Ruud, B.O., 1994. Seismic wave propagation in complex crust – upper mantle media using 2D finite difference synthetics, *Geophys. J. Int.*, **118**, 643-670.

Hestholm, S.O. and Ruud, B.O., 1994. 2D finite difference elastic wave modeling including surface topography, *Geophysical Prospecting*, **42**, 371-390.

Lacoss, R., Cunningham, R., Curtis, S., and Seibert, M., 1991. Artificial neural networks for seismic interpretation, *Technical Report, ESD-TR-91-170*, MIT Lincoln Laboratory, Lexington, MA.

Mendi, C.D. and Husebye, E.S., 1994. Near real time seismic magnitude and moment measurements, *Annali di Geofisica*, **37**, 365-382.

Ringdal, F., and Kværna, T., 1989. A multi-channel processing approach to real time network detection, and threshold monitoring, *Bull. Seism. Soc. Am.*, **79**, 1927-1940.

Ruud, B.O., Grundt, Y., and Husebye, E.S., 1995. A comparison of tau-sum velocity-depth inversion for a perturbed and unperturbed model, m/s prepared for publication.

Sereno, T.J., Bratt, S.R., and Bache, T.C., 1988. Simultaneous inversion of regional wave spectra for attenuation and seismic moment in Scandinavia, *J. Geophys. Res.*, **93**, 2019-2035.

Sguazzero, P., Kindeland, M., and Kamel, A., 1989. Dispersion-Bounded Numerical Integration of the Elastodynamic Equations, *Proceedings of the ICOSAHOM Conference, Como, Italy, June, 1989*, pp. 165-172. North Holland Publishing Company, The Netherlands.

Simone, A. and Hestholm, S., 1995. Optimal absorbing boundary condition in 2D finite difference elastic wave modeling. Empirical study and comparison with exponential damping, m/s prepared for publication.

3 3D FD modeling of scattering from topographic relief

As in the 2D case, we expect that inclusion of topography at the free surface will lead to improved modeling of upper crust propagation effects. Of particular interest here is the scattering of seismic energy from body waves (P or S) into surface waves (mainly Rg). This phenomena have been extensively studied and documented using data from the NORESS array in south-eastern Norway (Bannister et al, 1990; Gupta et al, 1993; Hedlin et al, 1991, 1994). For our 3D FD modeling experiments we have obtained digital elevation data for an area of 100×100 km centered on the NORESS array. Due to the huge computer memory requirements of 3D FD methods, we have so far been restricted to a model of size $40 \times 40 \times 35$ km with 0.2 km sampling. The topography in the model area is shown in Fig. 1.

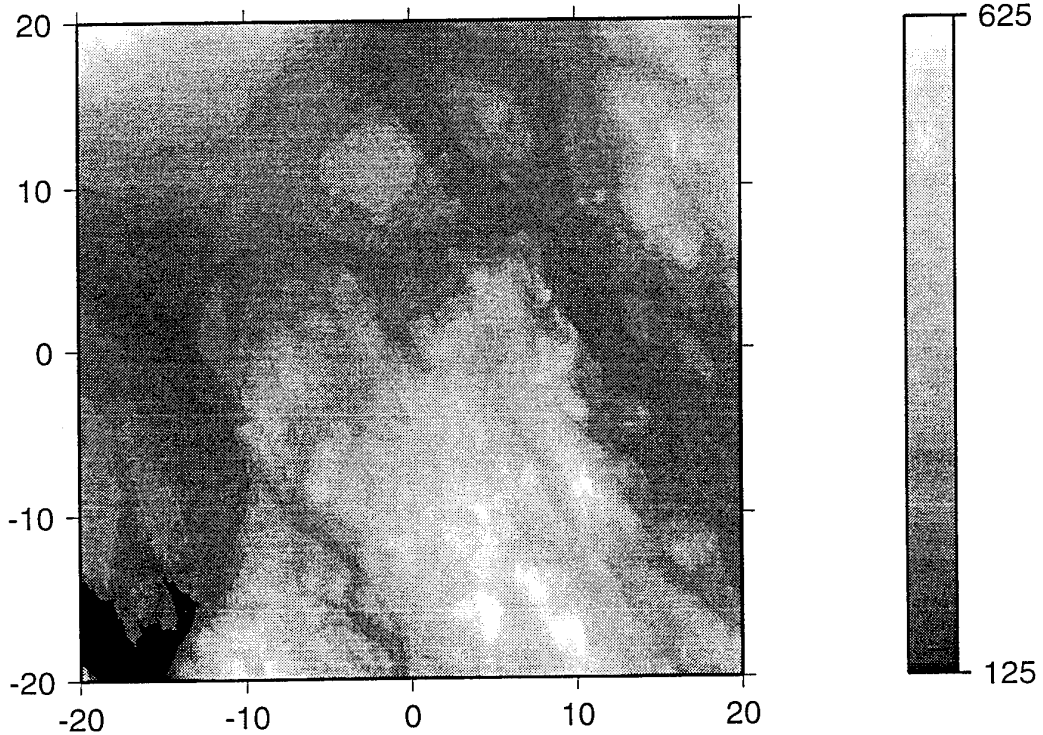


Figure 1: Topography in an 40×40 km area centered at the NORESS array. Horizontal axes are labeled in kilometers. Elevations are in meters above mean sea level. The dark area in the south-west corner of the figure is part of Lake Mjøsa (123 m above sea level).

The theoretical background for the implementation of 3D FD code with free surface topography is given in Appendix A. This method is a plane extension from 2D to 3D of the method described by Hestholm and Ruud (1994). The absorbing boundary condition used along the sides and bottom of the model is the socalled ‘exponential damping’ technique. A description of this method, and comparison with another method, is given in a paper by Simone and Hestholm (submitted for publication) included in Appendix B.

In all the examples shown here the incoming wave is a vertical incident plane P-wave simulating a teleseismic short period P-phase. The center frequency of the Ricker wavelet is 2.5 Hz, the P-wave velocity of the homogeneous medium is 6.0 km/s and the Poisson’s ratio is 0.25. The main problem encountered in our test runs is instabilities which start near the surface in an area of steep and rough topography. The instabilities appear as surface waves of exponentially increasing energy which slowly propagate out from the starting point. In order to quantify and locate areas which cause instabilities we have computed different functions depending on first and second order derivatives of the topography function $z = f(x, y)$. First, we computed the slope, i.e., the length of the topography gradient vector as

$$|\nabla f(x, y)| = \left[\left(\frac{\partial f}{\partial x} \right)^2 + \left(\frac{\partial f}{\partial y} \right)^2 \right]^{1/2}$$

Although the gradient of the topography is useful to define areas of strong scattering, the instabilities of the FD scheme is more likely related to its roughness. As a measure here we computed the Frobenius norm of the Hessian matrix of $f(x, y)$, i.e.,

$$\|H(x, y)\|_F = \left[\left(\frac{\partial^2 f}{\partial x^2} \right)^2 + \left(\frac{\partial^2 f}{\partial x \partial y} \right)^2 + \left(\frac{\partial^2 f}{\partial y \partial x} \right)^2 + \left(\frac{\partial^2 f}{\partial y^2} \right)^2 \right]^{1/2}$$

In Fig. 2 we show both $|\nabla f(x, y)|$ and $\|H(x, y)\|_F$ for the topography in Fig. 1. The derivatives were computed via Fourier transforms. In Fig. 2 there is a ‘wall’ of high gradient about 10 km east and 2 km north of the NORESS array (‘Bronkeberget’, Bannister et al, 1990). This area also have the roughest topography. The area close to Lake Mjøsa in the south-west corner is within the absorbing boundaries (thickness 4 km) of our FD modeling scheme and was therefore not properly modeled here.

3.1 Results and discussion

The first modeling attempt with unsmoothed real topography gave very unstable results (infinite amplitude) within a second after the wave front reached the surface. In our next attempt the elevations were first multiplied by 0.5 in order to reduce the topography. The results were stable and this is also consistent with 2D FD modeling results. In the latter case an east-west profile running through NORESS was unstable with real topography but stable with half elevations. Snapshots of the wavefield (vertical component of the particle velocity) at the free surface is shown in Fig. 3.

A dominant feature of these snapshots is the low-frequency/long-wavelength artificial reflections from the absorbing boundaries. Although we consider the exponential damping technique to be the most efficient absorbing boundary method we have tested, the case of an wave incident at an angle close to 90° with the boundary is the most difficult one. In our snapshots the artificial reflections are seen to generate surface waves starting at the absorbing boundaries, 4 km from the

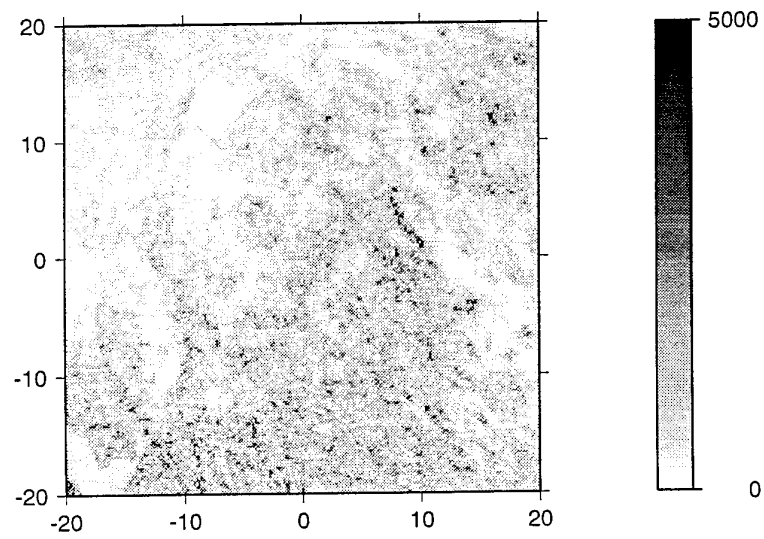
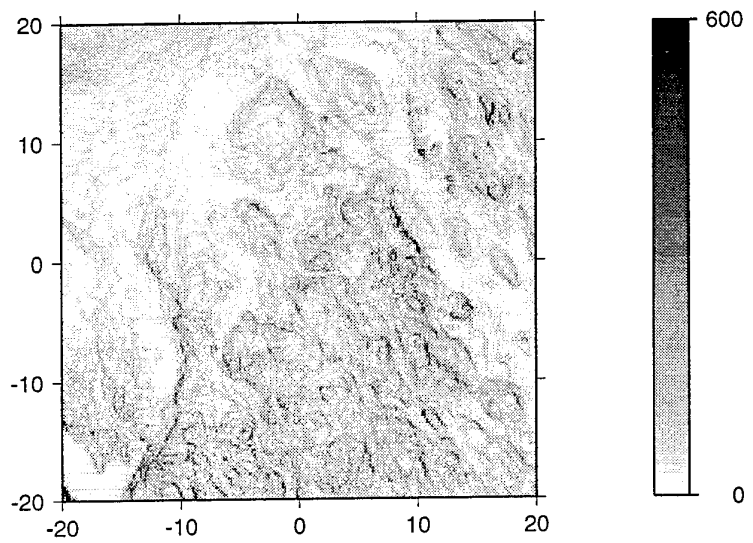


Figure 2: The absolute value of the gradient (upper part) and the Frobenius norm of the Hessian matrix (lower part) of the surface topography (Fig. 1). Horizontal lengths are in kilometers while elevations are in meters above so that the gradient is in m/km.

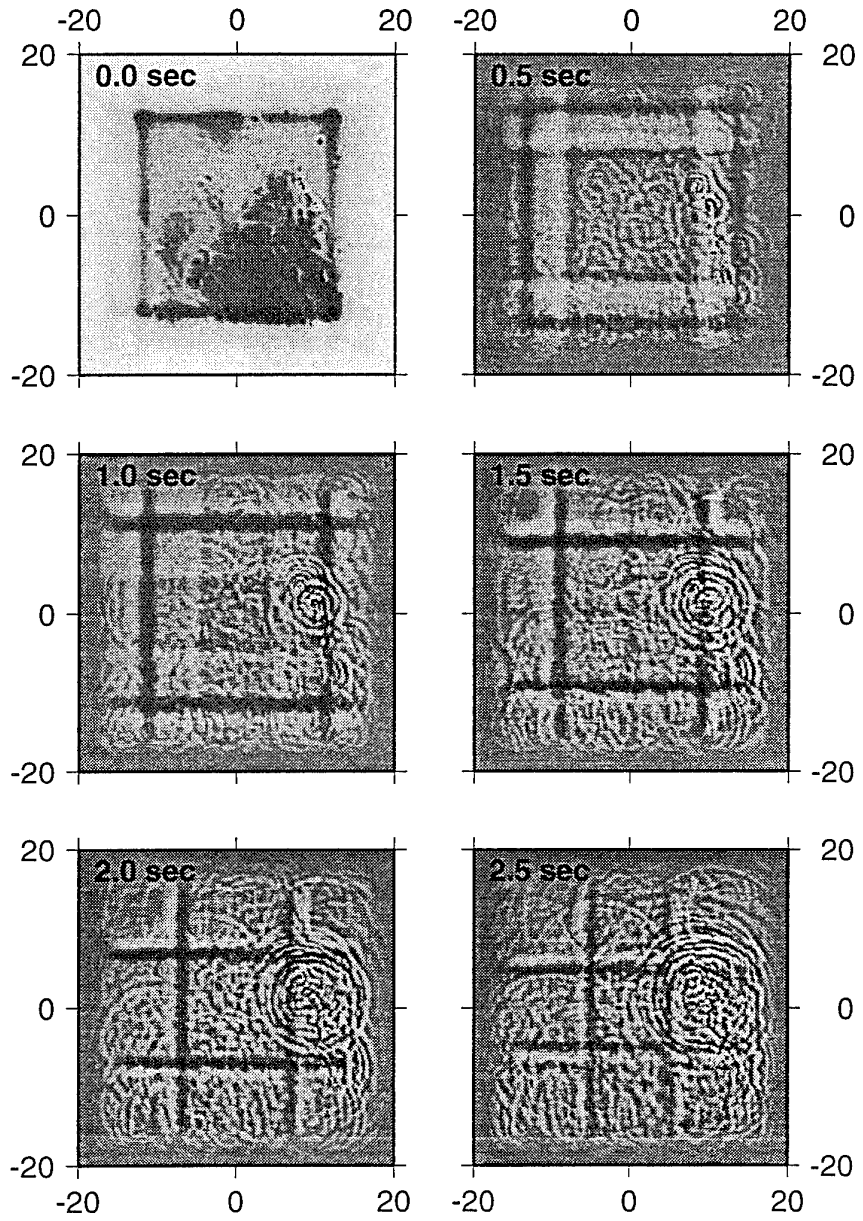


Figure 3: Snapshots of the vertical component of the particle velocity at the free surface. The time in the upper left corner of each snapshot is the time from when the plane vertical incident P-wave reached the surface. The first snapshot (at 0.0 sec) looks different from the others because the average amplitude differs from zero. The straight wavefronts parallel to the model boundaries are surface waves generated artificially from the absorbing boundaries. Note the strong scattering source located at Bronkeberget (2 km N, 10 km E) which is also highly prominent in real record analysis (Bannister et al, 1990).

edges of the model. Fortunately, the artificial reflections are frequency dependent, with longer wavelengths than most of the surface waves scattered by the topography, and can therefore be removed by image processing techniques. This have been done by applying a high-pass filter in 2D wavenumber domain which removes waves with wavelengths larger than 2.4 km and leaves waves with wavelengths less than 1.2 km – a cosine taper is used in the transition band. The snapshots after wavenumber filtering is shown in Fig. 4. As seen from this figure the scattered surface waves appear to radiate out from secondary point sources which coincide with areas of high topographic gradients (Fig. 1). The dominant scattering points are along the steep valley side east of ‘Bronkeberget’ about 10 km east of NORESS.

As the instabilities in our 3D FD modeling is likely due to the roughness of the free surface, we smoothed the topography to see if stable results could be obtained without reducing the elevation of the large scale topographic features. A low-pass version of the 2D wavenumber filter was used to smooth the topography. Several models were tested and it appeared that a rather high degree of smoothing was necessary to obtain stable results. The roughest topography model that seems to be stable was generated by removing all wavelengths shorter than 1.2 km – the cosine tapered transition band started at 2.4 km. The smoothed topography model is shown in Fig. 5 and its derivatives in Fig. 6. The snapshots computed for the new smoothed model are given in Fig. 7 and the filtered versions in Fig. 8. In this case the scattering points are also along a line about 10 km east of NORESS, but now extending further south compared to the unsmoothed (but reduced) topography. This result might be expected as also the gradient map (Fig. 6) exhibits this southward extension. However, more surprising is the fact that the scattered waves propagate mainly in the eastward direction – the unsmoothed model produced no distinct radiation pattern.

The amplitudes of the scattered waves were about the same in the two modeling experiments shown here. The gradients were also of the same size when we take into account that the values in Fig. 2 must be multiplied by 0.5 to be consistent with the model actually used. However, the Frobenius norm of the Hessian matrix (computed from the second order derivatives of the topography) is much smaller for the smoothed model. Also for other smoothed models (not as smooth as the one discussed here) for which the Frobenius norm was much smaller than for the reduced but unsmoothed model, the modeling gave instable results. It thus appear that the roughness of the topography is not the only reason for the instability or that another measure of the roughness is required. More work, including modeling with simpler ‘synthetic’ types of topography, is necessary in order to understand the origin of the instability and possibly eliminate the problem.

3.2 Concluding remarks

Even for small scale experiments 3D FD synthetic wavefield analysis provide as demonstrated here improved insight and a better understanding of surface scattering phenomenon. Particular gladdening is that the strong Rg scattering hill Bronkeberget, identified as such by Bannister et al. (1990) through analysis of NORESS recordings, can be realistically synthesized. Another interesting feature is that for certain spatial low-frequency variants of the local NORESS topography the wave propagation characteristics could change abruptly - the eastward only propagation of Rg-waves excited by secondary sources in the hilly Bronkeberget area. Such wavefield features are reminiscent of NORESS and GERESS recordings; at some sensors the Rg-phase is prominent while hardly visible at nearby sensors less than a kilometer away. In other words, also small scale

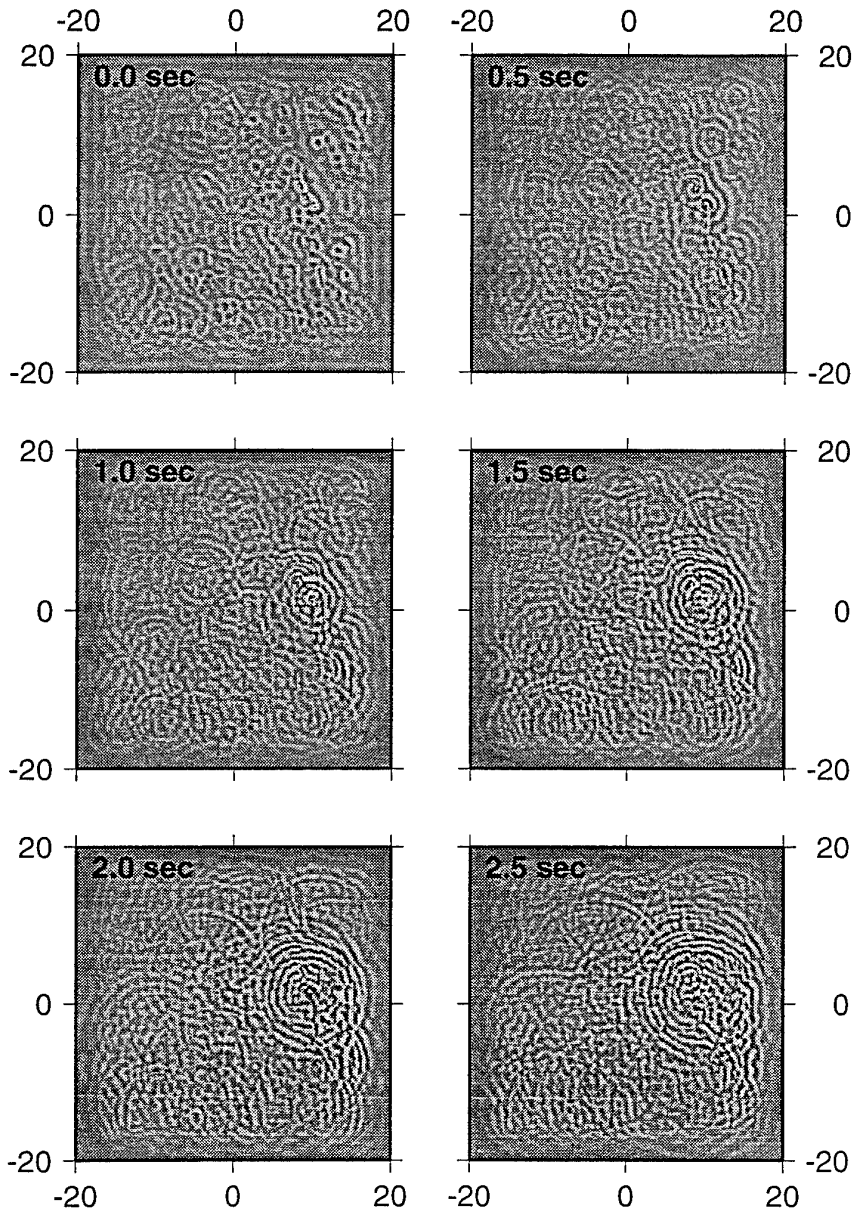


Figure 4: Wavenumber filtered versions of the snapshots in Fig. 3. The surface waves artificially generated at the absorbing boundaries are removed by high-pass filtering above 2.4 km wavelengths. The remaining surface waves are generated by scattering of the topographic relief (see Fig. 1). As in Fig. 3, the Bronkeberget scattering hill remains dominant.

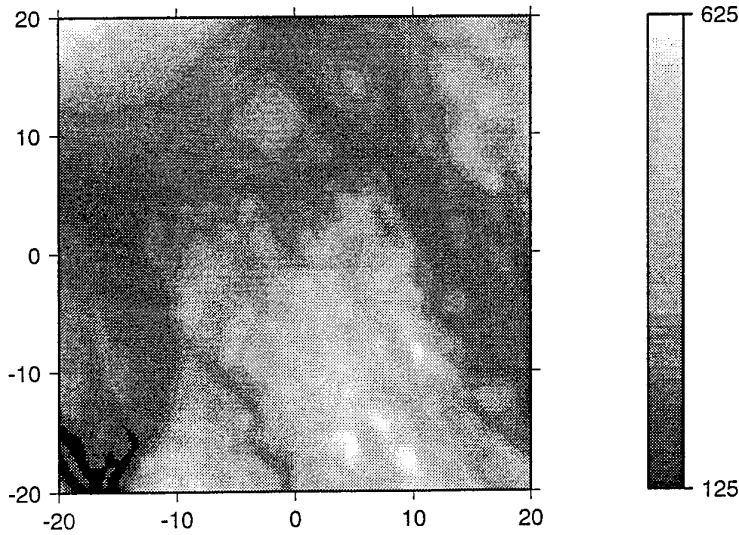


Figure 5: Smoothed topography in an 40×40 km area centered at the NORESS array obtained by 2D wavenumber filtering – a low-pass filter removing all wavelengths less than 1.2 km was used. Horizontal lengths are in kilometers while elevations are in meters.

crustal features may contribute to crustal blocking effects as often observed for Rg- and Lg-phases. Many of such wave field phenomena are out of range for 2D FD wave synthetic experiments hence our emphasize on continuous AFOSR contracted research efforts on 3D synthetic simulation of crustal wave field propagation.

Bent O. Ruud

Stig Hestholm

Eystein S. Husebye

References

Bannister, S.C., Husebye, E.S., and Ruud, B.O., 1990. Teleseismic P-coda analyzed by three-component and array techniques – deterministic location of topographic P-to-Rg scattering near the NORESS array, *Bull. Seism. Soc. Am.*, **80**, 1969-1986.

Gupta, I.N., Lynnes, C.S., and Wagner, R.A., 1993. An array study of the effects of a known local scatterers on regional phases, *Bull. Seism. Soc. Am.*, **83**, 53-63.

Hedlin, M.A., Minster, J.B. and Orcutt, J.A., 1991. Beam-stack imaging using a small aperture array, *Geophys. Res. Lett.*, **18**, 1771-1774.

Hedlin, M.A., Minster, J.B., and Orcutt, J.A., 1994. Resolution of prominent crustal scatterers near the NORESS small-aperture array, *Geophys. J. Int.*, **119**, 101-115.

Hestholm, S.O. and Ruud, B.O, 1994. 2D finite difference elastic wave modeling including surface topography, *Geophysical Prospecting*, **42**, 371-390.

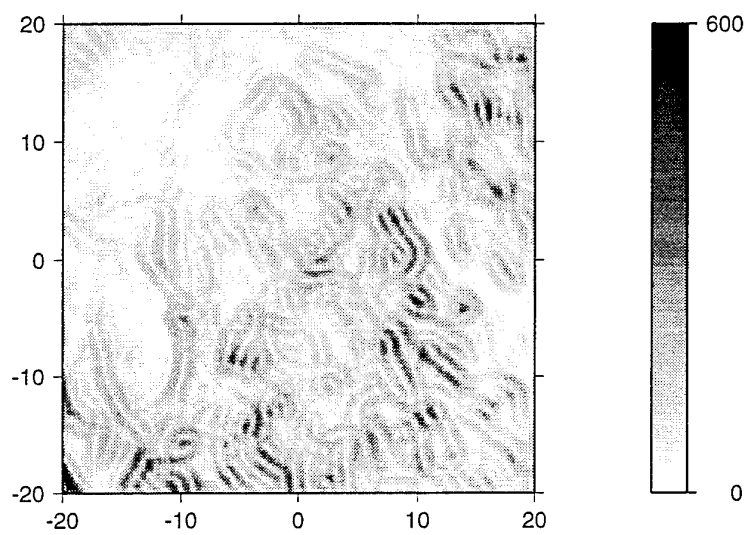
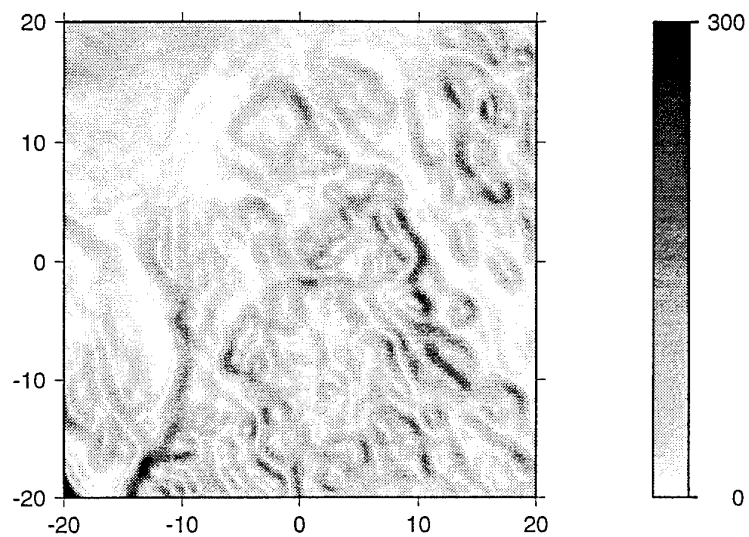


Figure 6: The absolute value of the gradient (upper part) and the Frobenius norm of the Hessian matrix (lower part) of the smoothed topography model (Fig. 5). Horizontal lengths are in kilometers while elevations are in meters above so that the gradient is in m/km.

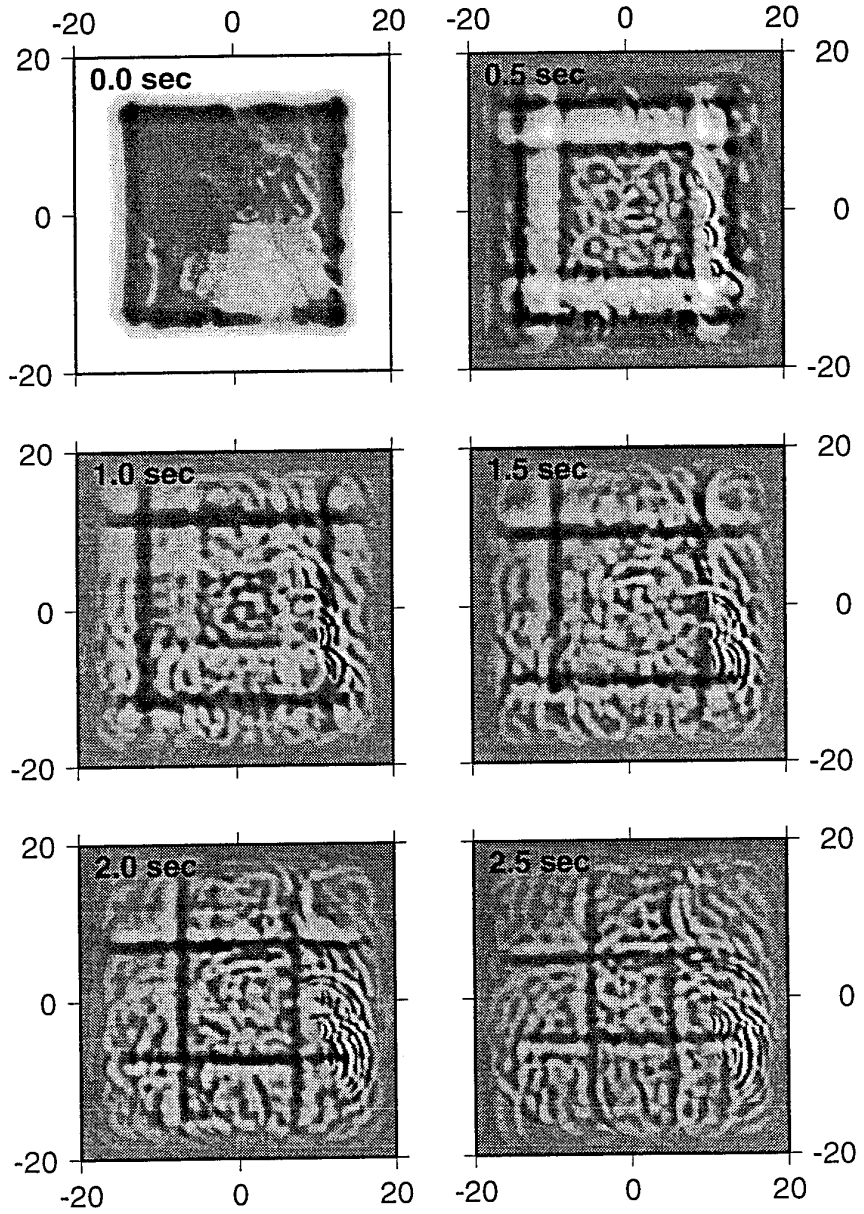


Figure 7: Snapshots of the vertical component of the particle velocity at the free surface computed for the smoothed topography model (Fig. 5). The first snapshot (at 0.0 sec) looks different from the others because the average amplitude differs from zero. The straight wavefronts parallel to the model boundaries are surface waves generated artificially from the absorbing boundaries. Note that the Bronkeberget scattering area (2 km N, 10 km E) produce strongly directional dependent (eastward propagating) Rg waves.

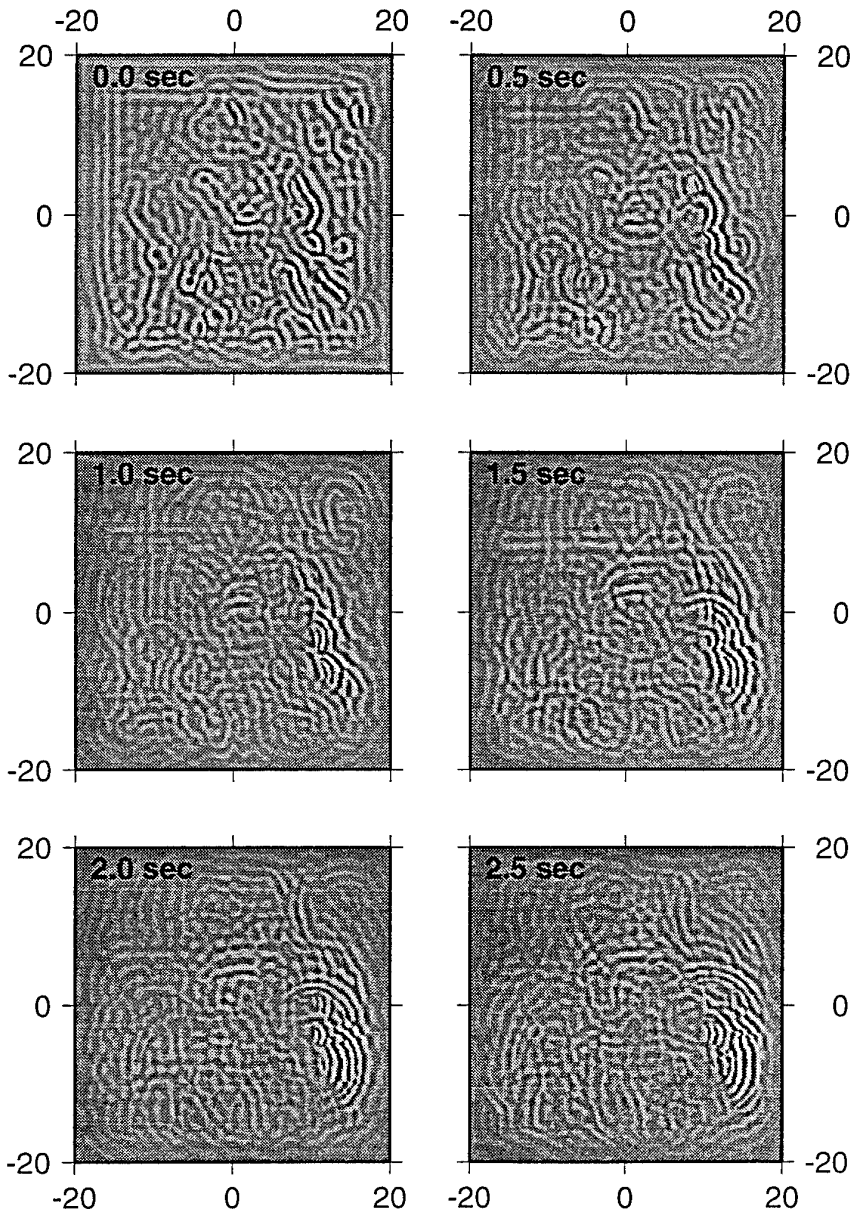


Figure 8: Wavenumber filtered versions of the snapshots in Fig. 7. The surface waves artificially generated at the absorbing boundaries are removed by high-pass filtering above 2.4 km wavelengths. The remaining surface waves are mainly generated by scattering of the smoothed topographic relief (Fig. 5).

Appendix A

Theoretical Background for 3D Finite Difference Elastic Wave Modeling including Surface Topography

Introduction

In this work explicit 3D boundary conditions for a free surface topography are deduced. The basis is the vanishing stress condition for a free surface. A 3D curved grid which is stretched in the vertical direction is used to adapt to the surface topography, i. e. the top surface of the grid coincides with the surface topography. A coordinate transform is used to transfer the elastic, isotropic wave equations from the curved to a rectangular grid in which the numerical computations are done.

At the topography surface, the velocity boundary conditions for a free surface are implemented into a local, rotated system at each point on the surface. Each of these systems has its vertical coordinate direction coinciding with the normal vector of the surface at the given point. The velocity boundary conditions are subsequently rotated back to the rectangular system. Once the boundary conditions are given in this system, the numerical computations can be performed.

In the following paragraphs, the 3D equivalents to the 2D equations given in Hestholm and Ruud (Geophysical Prospecting, 1994, 42:371-390) will be stated. Brief descriptions of the deductions will also be given. For each set of equations, the corresponding equation numbers for the 2D case in Hestholm and Ruud (1994) will be stated. In each instance, it

is possible to verify the coincidence between the 3D and the 2D case by eliminating either of the horizontal directions in 3D. Also stated is the coincidence between the conditions for the surface topography applied to a plane surface, and the plane surface conditions in 3D.

Elastic Wave Modeling Formulation

The linear transformation from the rectangular (ξ, τ, η) -system to the stretched (x, y, z) -system, where both systems have positive direction upwards along the vertical coordinate, can be written in 3D as (Hestholm and Ruud, 1994, eqs. (4) and (5))

$$x(\xi, \tau, \eta) = \xi, \quad (1')$$

$$y(\xi, \tau, \eta) = \tau, \quad (2')$$

$$z(\xi, \tau, \eta) = \frac{\eta}{\eta_{max}} z_0(\xi, \tau), \quad (3')$$

where $z_0(\xi, \tau)$ is the topography function.

The expressions for the partial derivatives corresponding to eqs. (8)–(10) in Hestholm and Ruud (1994), which are needed in the medium equations, are found to be

$$\frac{\partial \xi}{\partial x} = 1, \quad \frac{\partial \xi}{\partial y} = 0, \quad \frac{\partial \xi}{\partial z} = 0, \quad (4')$$

$$\frac{\partial \tau}{\partial x} = 0, \quad \frac{\partial \tau}{\partial y} = 1, \quad \frac{\partial \tau}{\partial z} = 0, \quad (5')$$

$$A(\xi, \tau, \eta) = \frac{\partial \eta}{\partial x} = -\frac{\eta}{z_0(\xi, \tau)} \frac{\partial z_0(\xi, \tau)}{\partial \xi}, \quad (6')$$

$$B(\xi, \tau, \eta) = \frac{\partial \eta}{\partial y} = -\frac{\eta}{z_0(\xi, \tau)} \frac{\partial z_0(\xi, \tau)}{\partial \tau}, \quad (7')$$

$$C(\xi, \tau) = \frac{\partial \eta}{\partial z} = \frac{\eta_{max}}{z_0(\xi, \tau)}. \quad (8')$$

We expand eqs. (1)–(3) in Hestholm and Ruud (1994) by the chain rule and put the dimension $J = 3$. Then we get the equations for the wave propagation inside the medium corresponding to eqs. (11)–(15) in the Hestholm and Ruud (1994),

$$\rho \frac{\partial u}{\partial t} = \frac{\partial \sigma_{xx}}{\partial \xi} + A(\xi, \tau, \eta) \frac{\partial \sigma_{xx}}{\partial \eta} + \frac{\partial \sigma_{xy}}{\partial \tau} + B(\xi, \tau, \eta) \frac{\partial \sigma_{xy}}{\partial \eta} + C(\xi, \tau) \frac{\partial \sigma_{xz}}{\partial \eta} + f_x, \quad (9')$$

$$\rho \frac{\partial v}{\partial t} = \frac{\partial \sigma_{xy}}{\partial \xi} + A(\xi, \tau, \eta) \frac{\partial \sigma_{xy}}{\partial \eta} + \frac{\partial \sigma_{yy}}{\partial \tau} + B(\xi, \tau, \eta) \frac{\partial \sigma_{yy}}{\partial \eta} + C(\xi, \tau) \frac{\partial \sigma_{yz}}{\partial \eta} + f_y, \quad (10')$$

$$\rho \frac{\partial w}{\partial t} = \frac{\partial \sigma_{xz}}{\partial \xi} + A(\xi, \tau, \eta) \frac{\partial \sigma_{xz}}{\partial \eta} + \frac{\partial \sigma_{yz}}{\partial \tau} + B(\xi, \tau, \eta) \frac{\partial \sigma_{yz}}{\partial \eta} + C(\xi, \tau) \frac{\partial \sigma_{zz}}{\partial \eta} + f_z, \quad (11')$$

$$\frac{\partial \sigma_{xx}}{\partial t} = (\lambda + 2\mu) \left(\frac{\partial u}{\partial \xi} + A(\xi, \tau, \eta) \frac{\partial u}{\partial \eta} \right) + \lambda \left(\frac{\partial v}{\partial \tau} + B(\xi, \tau, \eta) \frac{\partial v}{\partial \eta} + C(\xi, \tau) \frac{\partial w}{\partial \eta} \right), \quad (12')$$

$$\frac{\partial \sigma_{yy}}{\partial t} = \lambda \left(\frac{\partial u}{\partial \xi} + A(\xi, \tau, \eta) \frac{\partial u}{\partial \eta} + C(\xi, \tau) \frac{\partial w}{\partial \eta} \right) + (\lambda + 2\mu) \left(\frac{\partial v}{\partial \tau} + B(\xi, \tau, \eta) \frac{\partial v}{\partial \eta} \right), \quad (13')$$

$$\frac{\partial \sigma_{zz}}{\partial t} = \lambda \left(\frac{\partial u}{\partial \xi} + A(\xi, \tau, \eta) \frac{\partial u}{\partial \eta} + \frac{\partial v}{\partial \tau} + B(\xi, \tau, \eta) \frac{\partial v}{\partial \eta} \right) + (\lambda + 2\mu) C(\xi, \tau) \frac{\partial w}{\partial \eta}, \quad (14')$$

$$\frac{\partial \sigma_{xy}}{\partial t} = \mu \left(\frac{\partial v}{\partial \xi} + A(\xi, \tau, \eta) \frac{\partial v}{\partial \eta} + \frac{\partial u}{\partial \tau} + B(\xi, \tau, \eta) \frac{\partial u}{\partial \eta} \right), \quad (15')$$

$$\frac{\partial \sigma_{xz}}{\partial t} = \mu \left(\frac{\partial w}{\partial \xi} + A(\xi, \tau, \eta) \frac{\partial w}{\partial \eta} + C(\xi, \tau) \frac{\partial u}{\partial \eta} \right), \quad (16')$$

$$\frac{\partial \sigma_{yz}}{\partial t} = \mu \left(\frac{\partial w}{\partial \tau} + B(\xi, \tau, \eta) \frac{\partial w}{\partial \eta} + C(\xi, \tau) \frac{\partial v}{\partial \eta} \right), \quad (17')$$

where ρ is the density and λ and μ are Lamé's parameters. f_x , f_y and f_z are the components of the body forces, and u , v and w are the particle velocity components. σ_{xx} , σ_{yy} , σ_{zz} , σ_{xy} , σ_{xz} and σ_{yz} are the stress components.

Free Surface Boundary Conditions

The 3D free boundary conditions on the velocities at a locally horizontal surface (or where the z -axis coincides with the local normal vector of the surface) resulting from the vanishing

stress condition can be written

$$\frac{\partial u}{\partial z} = -\frac{\partial w}{\partial x}, \quad (18')$$

$$\frac{\partial v}{\partial z} = -\frac{\partial w}{\partial y}, \quad (19')$$

$$\frac{\partial w}{\partial z} = -\frac{\lambda}{\lambda + 2\mu} \left(\frac{\partial u}{\partial x} + \frac{\partial v}{\partial y} \right), \quad (20')$$

with x and y the horizontal coordinates and z the vertical coordinate. These equations correspond to eqs. (16) and (17) in Hestholm and Ruud (1994).

We want to apply these conditions to a topography surface. At each surface point, they then have to be imposed into a local coordinate system (x', y', z') in which the z' -axis coincides with the local normal vector of the surface. In this local system we impose the conditions (18')–(20'). Once this is done, they have to be rotated back to the rectangular system (ξ, τ, η) in order to do the numerical computations. This rotation is expressed by

$$\vec{v} = \mathbf{A} \vec{v}', \quad (21')$$

where \vec{v} and \vec{v}' are the particle velocity vectors in the (ξ, τ, η) - and the (x', y', z') -systems respectively. \mathbf{A} is the rotation matrix. This was found by geometrical considerations, and is given by

$$\mathbf{A} = \begin{pmatrix} \cos \theta & 0 & \sin \theta \\ -\sin \theta \sin \phi & \cos \phi & \cos \theta \sin \phi \\ -\sin \theta \cos \phi & -\sin \phi & \cos \theta \cos \phi \end{pmatrix}. \quad (22')$$

θ is the rotation angle between the ξ -axis and the local x' -axis in the (ξ, η) -plane. ϕ is the rotation angle between the τ -axis and the local y' -axis in the local (y', z') -plane. We also have the relations $\tan \theta = \partial z_0(\xi, \tau) / \partial \xi$ and $\tan \phi = \partial z_0(\xi, \tau) / \partial \tau$.

Now the calculations of the rotation from the (x', y', z') -system back to the (ξ, τ, η) -system are performed in a completely analogue way as is done in Appendix 3 of Hestholm

and Ruud (1994) for the 2D case. We arrive at the 3D boundary conditions for a free surface topography given in the computational (ξ, τ, η) -system by

$$\begin{aligned} \left(\frac{d^2}{q} + 1 \right) \frac{\partial u}{\partial \eta} &= d \left(1 - \frac{1}{q} \right) \frac{\partial u}{\partial \xi} - (d^2 r + p) \frac{\partial v}{\partial \xi} - (d^2 q + 1) \frac{\partial w}{\partial \xi} + \frac{p}{e} \frac{\partial u}{\partial \tau} \\ &\quad - \frac{d}{e} p r \frac{\partial v}{\partial \tau} - \frac{d}{e} r \frac{\partial w}{\partial \tau} + d(r - p) \frac{\partial v}{\partial \eta} + d(q - 1) \frac{\partial w}{\partial \eta}, \end{aligned} \quad (23')$$

$$\begin{aligned} (e p^2 + 1) \frac{\partial v}{\partial \eta} &= d f \frac{p}{q} \frac{\partial u}{\partial \xi} + (d + f p^2) \frac{\partial v}{\partial \xi} + p(f - d) \frac{\partial w}{\partial \xi} - \frac{d}{q} \frac{\partial u}{\partial \tau} \\ &\quad + p \left(\frac{1}{e} - 1 \right) \frac{\partial v}{\partial \tau} - \left(\frac{p^2}{e} + 1 \right) \frac{\partial w}{\partial \tau} \\ &\quad - f \frac{p}{q} \frac{\partial u}{\partial \eta} + p(1 - e) \frac{\partial w}{\partial \eta}, \end{aligned} \quad (24')$$

$$\begin{aligned} \left(\frac{\lambda}{\lambda + 2\mu} \left[d^2 \frac{1}{q} + \frac{1}{e} p^2 \right] - 1 \right) \frac{\partial w}{\partial \eta} &= \frac{1}{q} \left(\frac{\lambda}{\lambda + 2\mu} \frac{1}{q} - d^2 \right) \frac{\partial u}{\partial \xi} - d p \left(\frac{\lambda}{\lambda + 2\mu} \left[\frac{1}{q} + \frac{1}{e} \right] + 1 \right) \frac{\partial v}{\partial \xi} \\ &\quad + d \left(\frac{\lambda}{\lambda + 2\mu} \left[\frac{1}{e} p^2 - \frac{1}{q} \right] - 1 \right) \frac{\partial w}{\partial \xi} - \frac{d}{e} \frac{p}{q} \frac{\partial u}{\partial \tau} \\ &\quad + \frac{1}{e} \left(\frac{\lambda}{\lambda + 2\mu} \frac{1}{e} - p^2 \right) \frac{\partial v}{\partial \tau} + \frac{1}{e} p \left(- \frac{\lambda}{\lambda + 2\mu} \frac{1}{e} - 1 \right) \frac{\partial w}{\partial \tau} \\ &\quad + d \frac{1}{q} \left(\frac{\lambda}{\lambda + 2\mu} \frac{1}{q} + 1 \right) \frac{\partial u}{\partial \eta} \\ &\quad + p \left(\frac{\lambda}{\lambda + 2\mu} \left[\frac{1}{e} - d^2 \frac{1}{q} \right] + 1 \right) \frac{\partial v}{\partial \eta}. \end{aligned} \quad (25')$$

with

$$d = \frac{\partial z_0(\xi, \tau)}{\partial \xi}, \quad (26')$$

$$e = \cos \left[\arctan \left(\frac{\partial z_0(\xi, \tau)}{\partial \xi} \right) \right], \quad (27')$$

$$f = \sin \left[\arctan \left(\frac{\partial z_0(\xi, \tau)}{\partial \xi} \right) \right], \quad (28')$$

$$p = \frac{\partial z_0(\xi, \tau)}{\partial \tau}, \quad (29')$$

$$q = \cos \left[\arctan \left(\frac{\partial z_0(\xi, \tau)}{\partial \tau} \right) \right], \quad (30')$$

$$r = \sin \left[\arctan \left(\frac{\partial z_0(\xi, \tau)}{\partial \tau} \right) \right]. \quad (31')$$

Numerical Discretization

For the numerical discretization, the reader is referred to the corresponding paragraph in Hestholm and Ruud (1994). The same spatial and time discretization procedures are used as in the 2D case. In order to get explicit expressions for each physical variable at each time step, we still have to stagger the vertical velocity component w one half grid length downwards. Corresponding numerical definitions have to be implemented. The 3D boundary conditions eqs. (23')–(25') are discretized by second order, central, staggered finite difference operators. Below the free surface, the operator order is gradually increased with depth up to 8th order. Generally, u is staggered one half grid length in the positive ξ -direction, v is staggered one half grid length in the positive τ -direction, while w is staggered one half grid length in the negative η -direction (downwards).

To find the velocity components at the surface topography from the conditions (23')–(25'), we solve directly a simultaneous 3X3 system by using Cramer's rule. The vertical grid level for which the conditions are solved are not consistent for all the terms and equations, with up to a grid length difference vertically. As for the 2D case, this seems just to smooth the boundary to some extent, and even be to some advantage numerically.

Appendix B

Optimal Absorbing Boundary Condition in 2D Finite Difference Elastic Wave Modelling. Empirical Study and Comparison with Exponential Damping

A. Simone¹ and S. Hestholm^{2,3}

¹ Istituto Universitario Navale, Via Amm. Acton 38, Naples, Italy

² IBM Bergen, Ø. Kråkenes 17, 5042 Fjøsanger, Norway

³Now at Institute of Solid Earth Physics, Univ. of Bergen, Norway

Introduction

The problem of artificial reflections from grid boundaries in the numerical discretization of elastic and acoustic wave equations has intrigued geophysicists for a long time. Even if modern computers have made it possible to extend the synthetics over more wavelengths, equivalent to larger propagation distances, efficient absorption methods are still needed in order to minimize interference from artificial grid boundary reflections. In this study we examine the relative merits of a recently published absorption method, namely the Optimal Absorbing Boundary Condition (OABC) designed by Peng and Toksøz (1994) for 2D and 3D acoustic and elastic wave modelling. As a basis for comparison we use the Exponential Damping (ED), in which velocities and stresses are multiplied by progressively decreasing terms towards the edges. The experiment design is to implement both the OABC and the ED in our 2D finite difference elastic wave algorithm, see Hestholm and Ruud (1994), and then check their respective performances. A disadvantage with ED is that "absorption strips" are involved, which means in case of 3D modelling, that a significant amount of additional computer storage is required. On the other hand, initially we had some problems with the implementation of the OABC into our 2D finite difference scheme, because instabilities occurred in the synthetic wavefield calculations. Ways to

delay the occurrence of these instabilities will be addressed, in addition to the relative merits of the OABC and ED methods.

2-D finite difference implementation

The 2D finite difference scheme employed solves the basic equations governing wave propagation in an elastic isotropic medium, using the velocity-stress formulation, (Hestholm and Ruud, 1994). The discretization of the elastodynamic equations, with two staggered numerical space differentiators, has been applied as in Levander (1988). Details of the numerical discretization are given by Sguazzero *et al.* (1989). Spatial partial differentiation is achieved by finite difference operators on a staggered grid. The scheme used in the interior of the computational domain is accurate to the 8th order in space. For time stepping a leap frog technique is used.

The method of OABC extrapolates values on the numerical boundaries of a finite difference domain. It is expressed as a linear combination of wave fields at previous time steps and/or interior grids, and it makes use of the zeros and poles of the reflection coefficients in the complex plane. Peng and Toksøz (1994) pointed out that the purpose of the OABC was to design an absorbing boundary condition that was optimal in the sense that “maximum absorbing effects can be achieved with a minimum amount of computation and storage, and is easily implemented”. Approaching the boundaries, including the free surface, we apply successively lower order of the central, staggered finite difference operators used for discretizing the spatial derivatives. OABC is used at the bottom and sides of the grids. It is worthwhile to note that in the discretization we had to define the variables at each grid point in such a way that we did not make use of the corners of the computational domain.

ED involves, as mentioned, some restrictions on the computational storage. Applying this method, it is necessary to preserve strips along the boundaries of the computational domain and to introduce damping mechanisms there. The exponential damping consists of multiplying each physical variable in the strip by $\exp(-(\text{ac} * \text{idist})^2)$, where **idist** is the current number of grid points to the first grid point of absorption, and **ac** is a constant equal to 0.015 in our case. Damping is enforced within absorption strips of 20 grid points along the

bottom and the sides of the grid, while gradual decrease of the spatial finite difference order is applied only when approaching the free surface. In both methods, boundary conditions as for a plane free surface are used at the upper boundary of the domain.

Results

In our numerical tests the model size is 100 km by 70 km, with 351 grid points vertically and 501 grid points horizontally. The grid length in both directions is 200 m. A pressure wave is initiated from a Gaussian point source with a central frequency of 2.5 Hz. We chose an upper bound of 1.5% for the relative error of the numerical group velocity. This requires 3 samples per shortest wavelength in case of the 8th order operator used. Furthermore, two different medium models are tested; a homogeneous one where the P-velocity is constant, and a stratified one where the medium P-velocities are constant within each layer.

In connection with our use of higher order finite differences for spatial discretization, we found that the OABC became unstable for long time simulation runs. This result was confirmed by extensive numerical testing, including long computer runs, i.e. 18376 time steps, which means about 75 seconds of wavefield synthetics. Initially we used 8th order of accuracy in the interior of the domain and then second order along three levels next to the absorbing boundaries (thus a very sharp discontinuity in the order of accuracy). We got instabilities after $O(100)$ time steps; instability started either along the absorbing boundaries or at the corners at the bottom of the computational grid. From there it spread out and destroyed the synthetics.

Peng and Toksøz (1994) gave some examples of 3D elastic finite difference runs where OABC was used. The employed scheme had fourth order accuracy in space and second order accuracy in time. Elastic wave propagation in an unbounded homogeneous medium were simulated, and the results were stable.

Thus for a realistic test of OABC using our scheme it was natural to lower the spatial finite difference order. That choice led to successful runs whether using 2nd order finite difference operators all over the grid or using 4th order; in both cases we got completely stable runs, but the penalty was a larger numerical dispersion.

So how to get a better performance for our higher order scheme, in implementing OABC, in terms of both accuracy and stability? We solved the problem by decreasing gradually the finite difference order when approaching the boundaries. It was a matter of experimentation to find the proper number of grid points near the boundaries on which to apply a certain finite difference order. It seems important to use exactly two 2nd order grid points near the boundaries, and then to increase the number of grid points at which higher order finite differences are used.

In our discretization we arrived at a total number of 12 grid points for which to lower gradually the finite difference order. We used 8th order in the interior of the grid, then 6th, 4th and 2nd order as approaching the boundaries. In this way we managed to run for at least 14000 time steps (about 60 seconds of simulated time) before a slowly growing instability started appearing along the absorbing boundaries. Simulated wavefields for such large time laps implies that the most interesting wave phenomena are adequately synthesized.

Peng and Toksøz (1994) mentioned the importance of stability in the choice of an absorbing boundary condition. As an example, they mentioned that Emerman and Stephen (1983) demonstrated that the boundary condition of Clayton and Engquist (1977) was unstable for a wide range of elastic parameters, and further that Mahrer (1986) found the boundary condition of Reynolds (1978) to be unstable as well. Peng and Toksøz made a comparison, using a 4th order spatial finite difference scheme in 3D, between the OABC, Reynolds' and Higdon's (1990) boundary conditions. They found that the OABC had less artificial reflections than the two latter schemes. Thus our study may be considered a further test of absorbing boundary conditions.

In order to compare the artificial reflections using both the OABC and the ED, two different types of models were used. The first model is homogeneous with a constant P-velocity of 7.1 km/s. The second model is a multilayer realization of the crust and upper mantle consisting of several constant velocity layers (Fig. 5). In all cases the S-wave layer velocity is related to the P-wave velocity via Poisson's ratio; by this choice the densities are linear functions of the P-velocities. At the top of the model free surface boundary conditions are implemented. A Gaussian point source is located 50 km from the left edge of the grid and 500 m below the surface.

For the first two runs the homogeneous medium model was used, the first one using the OABC (Figs 1 and 2) and the second one the ED (Figs 3 and 4). In Fig. 1 the velocity vector modulus is displayed in a snapshot 11 s after a pressure wave has been initiated. We see that the P wave front at this time has just hit the bottom of the model. The snapshot reveals a weak P-P reflection from the bottom, while from both sidewalls stronger artificial P-P and P-S reflections can be noticed. Interestingly, the reflections from the left sidewall are stronger than the ones from the right sidewall. The reason for this is, as mentioned by Levander (1988), that we make use of two staggered numerical space differentiators and a staggered grid definition of the field variables. The consequence is that not exactly the same variables are being absorbed at each boundary. Experiments aimed at rectifying this deficiency of asymmetric reflections were done by using the OABC to absorb every variable at its outermost defined point, but that produced even stronger grid boundary reflections.

In Fig. 2 the velocity vector modulus is displayed in a snapshot 22 s after the pressure wave has been initiated. We see mainly artificial reflections here, since the dominant non-artificial wavefield has passed out of the model frame. The reflections from the S-wave are stronger than from the P-wave, and correspond to our choice of maximum P-wave absorption (Peng and Toksøz, 1994). The strongest reflections are seen to come from the bottom, while the vertically oriented wave front seen near the right boundary is the P-wave reflection from the left boundary.

Figs 3 and 4 are similar to Figs 1 and 2 respectively, except that in this case ED was applied within strips of 20 grid points along the numerical boundaries at the bottom and sides. Clearly, the ED scheme works better than the OABC in absorbing both P-waves and S-waves. It absorbs equally well along the bottom and the sidewalls. In Fig. 4 the non-artificial waves have passed out of the model, and only artificial grid reflections remain. They are weaker than reflections with the OABC by a factor of approximately 10^{-2} , and furthermore, the run is completely stable.

A homogeneous model is rather an oversimplification of the real Earth, and so further comparison between OABC and ED is tied to wavefield simulation using a multilayered crust - upper mantle model shown in Fig. 5. Velocity vector modulii as in Figs 1-4 are shown in Figs 6-9, but now with the background model of Fig. 5 added. This fact, together with the multiply additional reflections from the various layer boundaries, cause these snapshots to be less clear than those for the homogeneous medium model (Figs 1-4). Figs 6 and 7 show the wave field respectively 11 seconds and 22 seconds after the pressure wave was initiated, using OABC. Also in this case we see asymmetric P-P and P-S reflections from the sidewalls, together with a whole range of wave conversions and reflections from the various layers. The absorption at the bottom is seen to be somewhat better than that at the sidewalls. This is due to the staggered grid discretization.

Figs 8 and 9 show corresponding runs where we made use of ED. We see the same wave conversions and reflections as those of Figs 6 and 7 caused by the layered medium, but now less prominent. Along the numerical boundaries the absorption strips of 20 grid points' width are clearly visible. We get a confirmation again that the performance of ED is better than that of OABC. Comparing the results of the last two runs we found that the artificial reflections from using OABC were on the average $O(10)$ stronger than the ones using ED. Noteworthy, for the long runs using ED, the damping affects the resolution in the interior of the domain, slightly weakening the wave amplitudes. In this respect OABC behaves better.

Conclusions

In implementing the OABC we found the choice of spatial finite difference order to be important. It must be decreased when approaching the numerical boundaries in order to keep the run stable as long as possible. Our synthetic discretization scheme uses 8th order finite differences in the interior of the grid. Thus, moving from the interior towards the boundaries we found the following procedure to be optimal: 6 layers of 6th order finite differences, then 4 layers of 4th order and finally 2 layers of 2nd order next to the numerical boundary. Comparing the amount of numerical boundary reflections using OABC in relation to using ED, it seems clear that ED works better, even when applying it within a thin strip. The mentioned drawback of additional computer storage are offset by the smaller simulation time using ED.

Acknowledgements

IBM is acknowledged for use of its IBM RISC System/6000 550E. This research was supported by the Air Force Office of Scientific Research, USAF under Grant F4926-92-J-0510. A. S. acknowledges support from EU's COMETT student exchange programme. For the snapshots presented in this paper we acknowledge the use of PGraph produced by F. C. Lundbo and J. Petersen. This work is part of a project involving the Institute of Solid Earth Physics, University of Bergen, represented by prof. E. S. Husebye and scientist B. O. Ruud. We thank C. Peng for his kind provision of the source code of the OABC.

References

Clayton, R. and Engquist, B. , 1977. Absorbing boundary conditions for acoustic and elastic wave equations. *Bull. Seism. Soc. Am.* , **67**, 1529-1540.

Emeran, S. H. and Stephen, R. A. , 1983. Comment on absorbing boundary conditions for acoustic and elastic wave equations by R. Clayton and B. Engquist. *Bull. Seism. Soc. Am.* , **73**, 661-665.

Hestholm, S. O. and Ruud, B. O. , 1994. 2-D finite-difference elastic wave modelling including surface topography. *Geoph. Prosp.*, **42**, 371-390.

Higdon, R. L. , 1990. Radiation boundary conditions for elastic wave propagation. *SIAM J. of Num. Analysis*, **27**, 831-870.

Levander, A. R. , 1988. Fourth-order finite difference P-SV seismograms. *Geophysics*, **53**, 1425-1436

Mahrer, K. D. , 1986. An empirical study of instability and improvement of absorbing boundary conditions for the elastic wave equation. *Geophysics*, **51**, 1499-1501.

Peng, C. and Toksøz, M. N. , 1994. Optimal absorbing boundary conditions for finite difference modeling of acoustic and elastic wave propagation. *J. Acoust. Soc. Am.*, **95**, 733-745.

Reynolds, A. C. , 1978. Boundary conditions for the numerical solution of wave propagation problems. *Geophysics*, **43**, 1099-1110.

Sguazzero, P., Kindelan, M. and Kamel, A., 1989. Dispersion-bounded numerical integration of the elastodynamic equations with cost-effective staggered schemes. Proceedings of the ICOSAHOM conference, Como, Italy, 165-172. North-Holland Publishing Co.

FIGURE 1. Snapshot of velocity vector modulus 11 s after a pressure wave is initiated from a Gaussian point source at depth 500 m below the surface. The medium model is homogeneous and OABC is used.

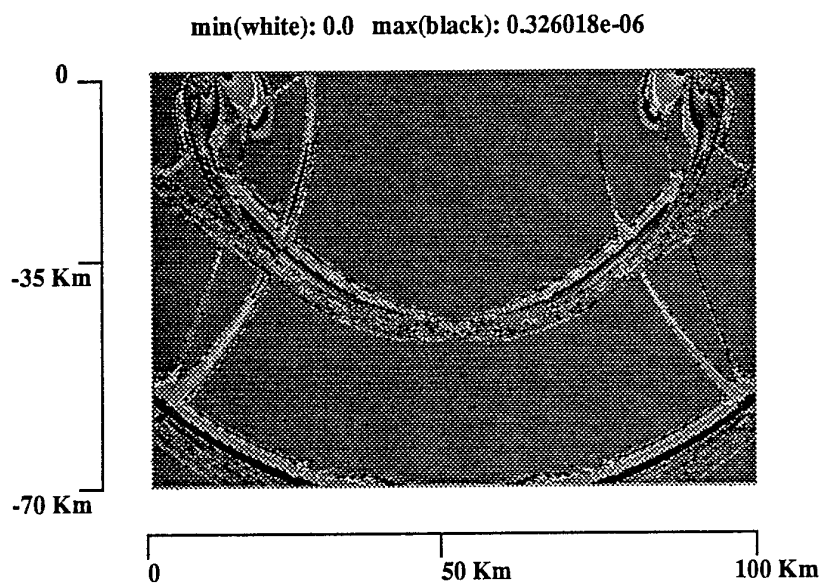


FIGURE 2. Snapshot of velocity vector modulus for the same situation as in Fig. 1, 11 seconds later.

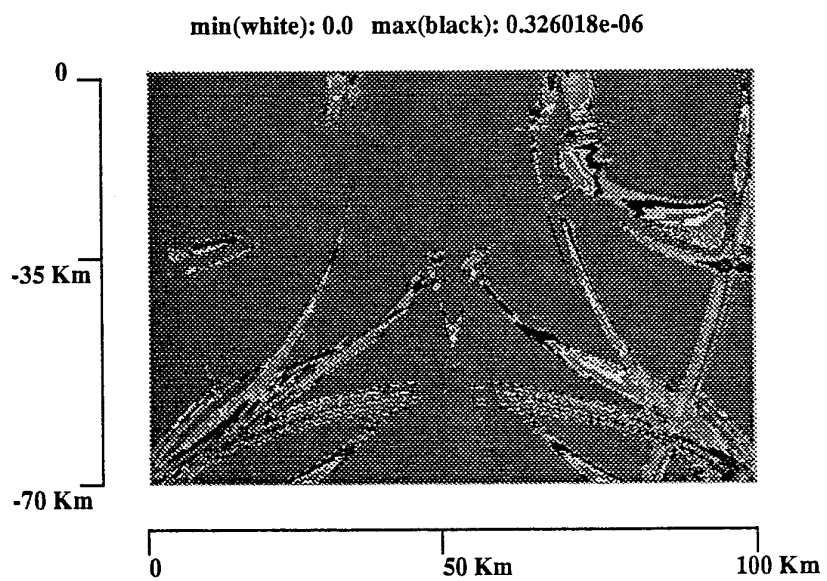


FIGURE 3. Snapshot of velocity vector modulus for the same situation as in Fig.1, but in this case ED is used.

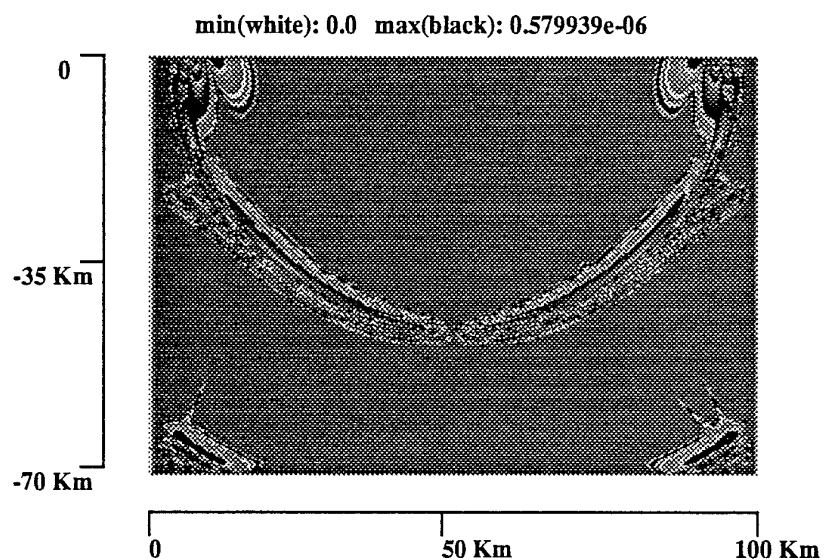


FIGURE 4. Snapshot of velocity vector modulus for the same situation as in Fig. 3, 11 seconds later.

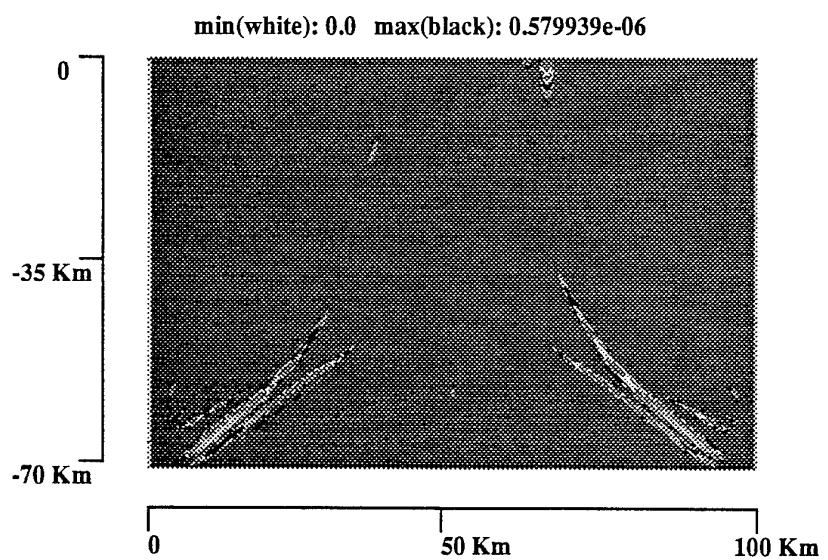


FIGURE 5. Snapshot of velocity vector modulus 1.2 s after a pressure wave is initiated from a Gaussian point source at depth 500 m below the surface. The source position and the background model of the layered medium are clearly visible. The maximum P-velocity is 8.18 km/s right below the Moho. The Moho is located at 35 km depth. The nearest layer above the Moho represents a P-velocity of 6.9 km/s. The next layer is the maximum velocity layer in the crust with a P-velocity of 7.1 km/s. Just below the surface there is the minimum velocity layer with a P-velocity value of 6.6 km/s.

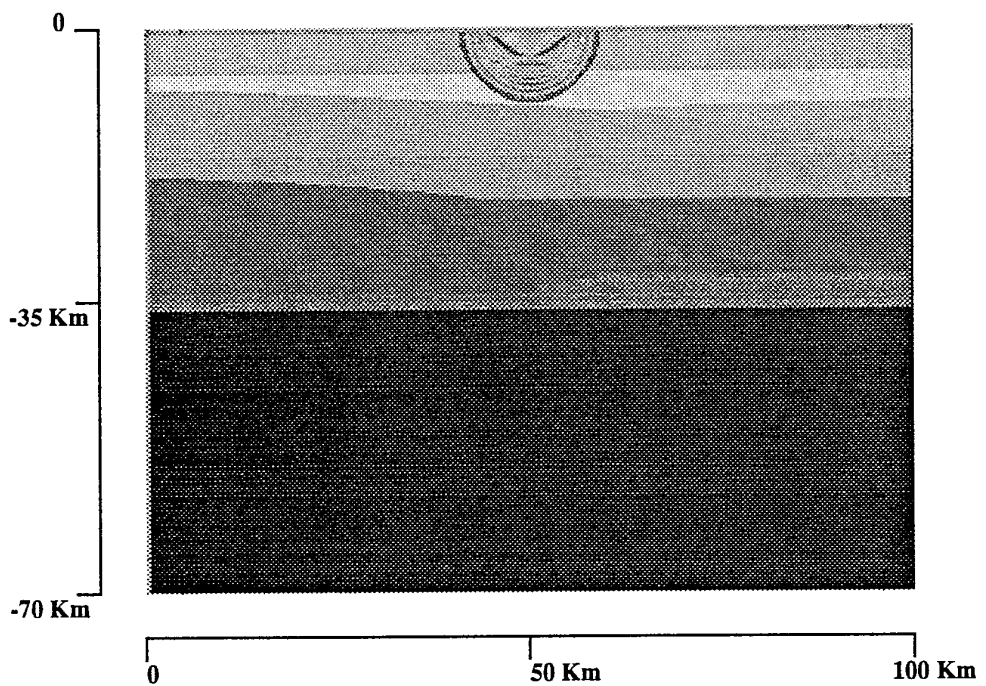


FIGURE 6. Snapshot of velocity vector modulus 11 s after a pressure wave is initiated from a Gaussian point source at depth 500 m below the surface. The medium model is layered and OABC is used.

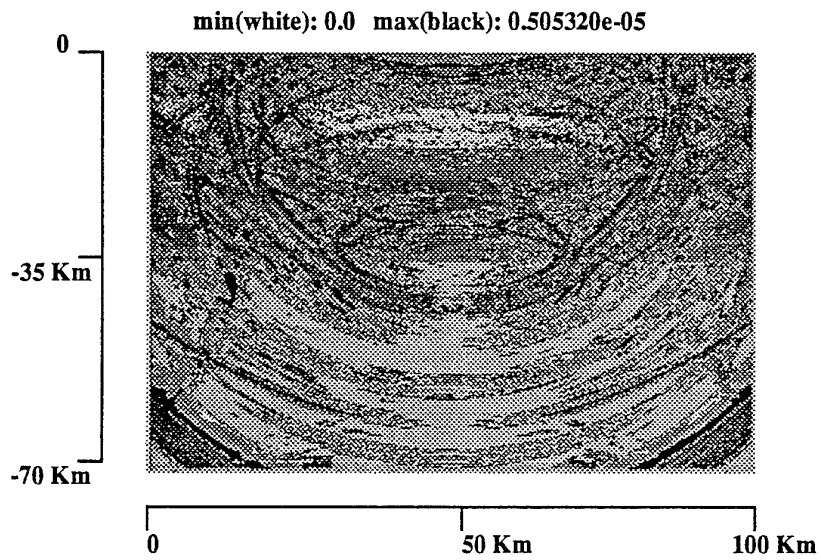


FIGURE 7. Snapshot of velocity vector modulus for the same situation as in Fig. 6, 11 seconds later.

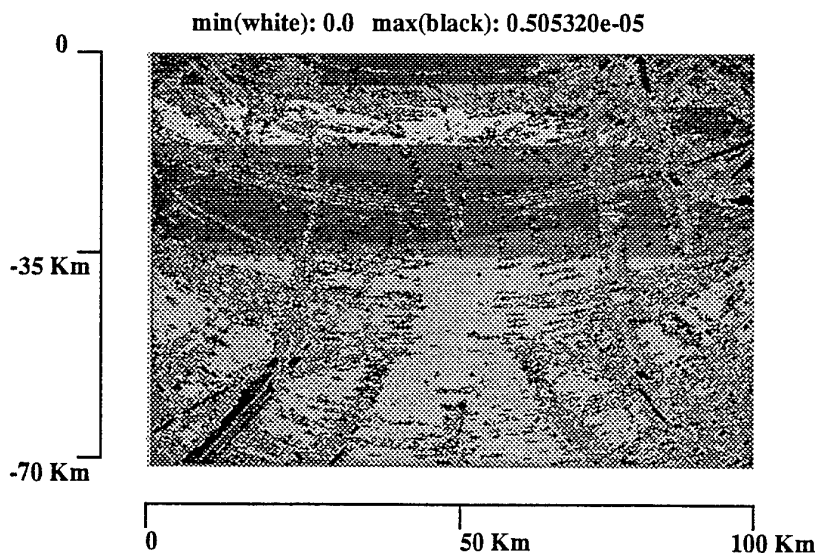


FIGURE 8. Snapshot of velocity vector modulus for the same situation as in Fig.6, but in this case ED is used.

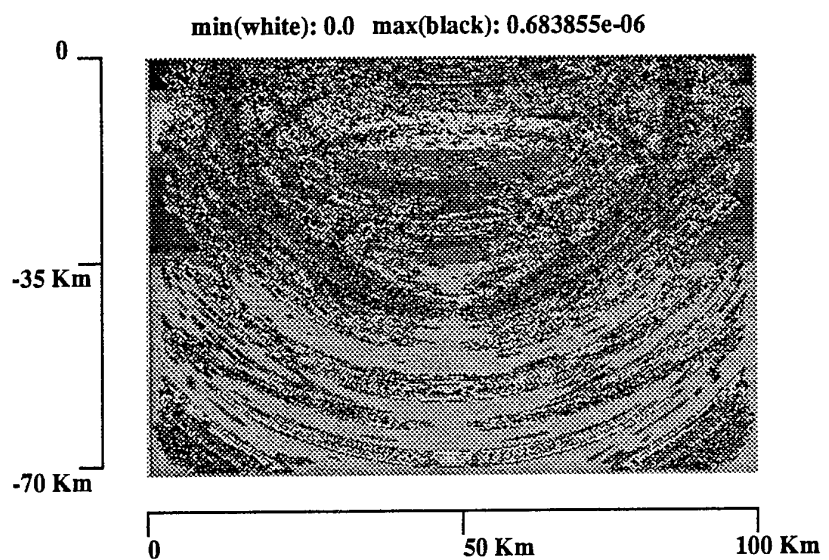
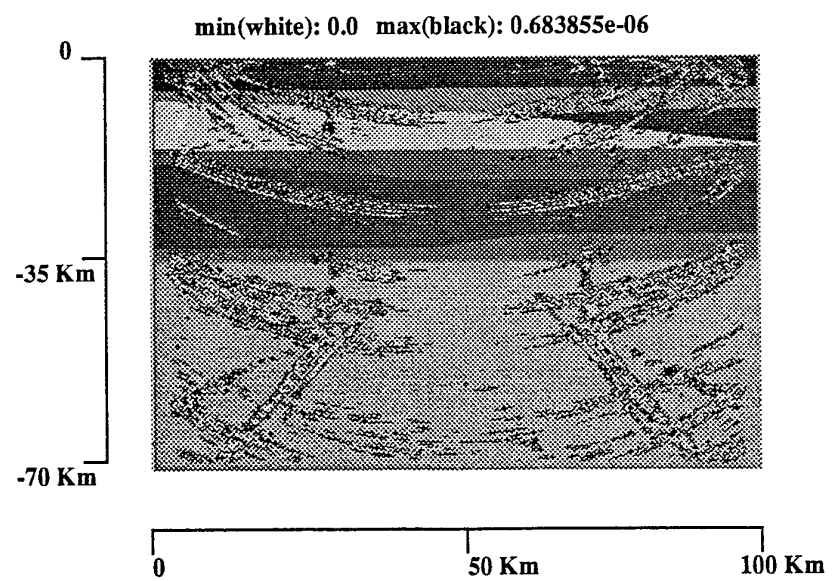


FIGURE 9. Snapshot of velocity vector modulus for the same situation as in Fig. 8, 11 seconds later.



Appendix C

A COMPARISON OF TAU-SUM VELOCITY-DEPTH INVERSION FOR PERTURBED AND UNPERTURBED CRUSTAL MODELS

An experiment with 2D finite difference synthetics

B.O. RUUD, Y. GRUNDT AND E.S. HUSEBYE

Institute of Solid Earth Physics

University of Bergen

Allégaten 41

N-5007 Bergen

Norway

1. Introduction

The transformation of seismic profiling data to the domain of intercept time and ray parameter ($\tau - p$) and the subsequent interpretation and inversion for velocity-depth models by the τ -sum method have become a popular processing technique in wide-angle marine seismic profiling (Stoffa et al., 1981; Diebold and Stoffa, 1981). The method offers several advantages:

- In processing:
The $\tau - p$ transformation is a beamforming process (plane wave decomposition) in which coherent events are enhanced and incoherent ones suppressed.
- In interpretation:
The τ -sum inversion method require that we identify and digitize the ‘principal branch’ in the $\tau - p$ domain consisting mainly of post-critical reflections and diving waves. Since post-critical reflections are totally reflected they have relatively large amplitudes compared to first arrivals which usually are head waves. Thus the problem of picking weak first arrivals (which is often a critical process when interpreting and inverting data in $x - t$ domain) is avoided.
- In Inversion:
The simple τ -sum travelttime inversion technique of Diebold and Stoffa (1981) is easy to implement and works both for discontinuous and continuous velocity-depth functions. Its main limitation is that the velocity must increase monotonically with depth.

Like many other inversion methods τ -sum is limited to laterally homogeneous models, i.e., an one-dimensional model in the sense that the velocity is a function of depth only. The case of dipping plane layer interfaces is discussed by Diebold and Stoffa (1981). In this paper we will examine the effect of relatively small scale inhomogeneities introduced in the form of random perturbations with a von Kármán autocorrelation function and an RMS of 3%. We generate synthetic data by a 2-dimensional 8-th order elasto-dynamic finite difference method (Hestholm et al., 1994; Sguazzeri et al., 1989) for both a laterally homogeneous and a perturbed model. The synthetic seismograms are transformed to $\tau - p$ domain, interpreted, and velocity-depth functions are computed for both models. Besides comparing the two resulting models we can also compare the data in both $x - t$ and $\tau - p$ domain.

2. Synthetic model and seismogram generation

The P-wave velocity-depth function of the unperturbed, laterally homogeneous model is given in Fig. 1. The crustal model consists of both constant velocity and gradient layer. The S-wave velocities were calculated by assuming a constant Poisson's ratio of 0.25. Densities were found from Birch's law.

For the finite difference computation we used a 340 km long and 70 km deep model. The grid step is 0.2 km and the source signature is a Ricker wavelet with a center frequency of 2.5 Hz (the data were bandpass filtered 1 to 4.5 Hz prior to processing). Absorbing boundaries are used at the sides and bottom of the model, while vanishing stresses are used at the free surface. The explosion source is placed 0.5 km below the surface 10 km from the left side of the model. The seismograms of 60 seconds duration are extracted at 800 points along the surface to the right of the source and with 0.4 km intervals.

The perturbed model was generated by scaling the unperturbed one with a 2D random field having a unit mean, a von Kármán autocorrelation function of order 0.3 (corresponding to a fractal dimension of 2.7), correlation distances of 10 km horizontally and 2.5 km vertically, and an RMS value of 0.03 (3%). The generation and use of stochastic field in seismic modelling is discussed in e.g., Frankel and Clayton (1981), Charrette (1991), and Holliger and Levander (1992). The choice of these model parameter is discussed in Hestholm et al. (1994), and is believed to be realistic in a crystalline continental crust environment. A section from our perturbed model is shown in Fig. 2.

3. Finite difference modelling results

The synthetic seismogram profiles are shown in Fig. 3 and 4 for the unperturbed and perturbed models respectively. In both cases the dominating phase (highest amplitude) is the fundamental mode Rayleigh wave (Rg) propagating with a group velocity of 3.15 km/s. For small offsets (say less than 30 km) the seismogram section from the unperturbed model is relatively easy to interpret. It consists mainly of the direct P-wave, the Rg phase and P reflections from the model discontinuities. With increasing offset we see a more complicated P wavetrain (coda) consisting of P-multiples and mixed waves, i.e., waves that have propagated partly as P and partly as S due to mode conversion at internal reflectors or at the free surface. These mixed waves will have apparent velocities in the same range as pure P-waves because in a laterally homogeneous model the ray parameter (slowness) will not change during reflections or transmission. At distances beyond about 145 km the Moho refracted Pn phase is the first arrival, but of relatively weak amplitude.

The ideal explosion source used in this modelling experiment does not generate S-waves when applied in a homogeneous unbounded medium, but because the source here is close to the surface (compared to wavelength) quite strong S-waves are generated in all directions except for the vertical. The S-coda looks simpler than the P-coda in this profile because in the distance range out to about 150 km (where we have an opportunity to observe the first part of the S-coda) the multiple S-phases have too high apparent velocities to be trapped in the crustal waveguide. However, at larger distances the S-multiples (constituting the Lg phase) have lower velocities (< 4.5 km/s) and thus propagate as guided waves.

The seismic profile from the perturbed model (Fig. 4) is very messy compared to Fig. 3. The P-wave reflections from the discontinuities in the original model are difficult to identify and look like coda waves even at short offsets. The Pn phase shows a variable amplitude, it is stronger than for the unperturbed model in some distance ranges and almost disappear at others. The P-coda is strong into the S-waves and masks most of the Sn phase. Much of the coda waves are seen to consist of waves propagating with Rg velocities and in both forward and backward directions. These scattered surface waves are generated when a strong primary wave hits strong heterogeneities near the free surface. Also in real recordings surface waves are seen to constitute a significant part of the coda (see e.g., Hestholm et al., 1994).

4. $\tau - p$ transformation

The subsequent processing of the synthetic dataset was performed using the ProMAX commercial processing system. Prior to $\tau - p$ transformation a $f - k$ filter was applied in order to remove the dominating Rg-wave. The fan-shaped $f - k$ filter rejected all waves with apparent velocities less than 3.33 km/s. With the small intersensor interval of 0.4 km for this profile, spatial aliasing is not a problem for the frequencies of interest, i.e., less than 4.5 Hz. In order to avoid artifacts in the transformed data due to truncation effects we also found it necessary to mute the data both in time and space. A 5 sec long ramp function was used at the end of each seismogram, and similarly a 20 km long ramp function was used to gradually weight down the seismograms at the end of the profile.

The resulting $\tau - p$ transformed datasets are shown in Fig. 5 and 6 for the unperturbed and perturbed model respectively. As for the time-offset profiles there is a great difference between the models. Although Fig. 5 is rather complicated with both P-, S- and mixed-waves, the different phases forms distinct branches in $\tau - p$ domain and most of these are easily explained after some consideration. As expected the reflected P-waves forms quarter-ellipses in the upper left hand corner of the figure (τ range 0 – 11 s and p range 0 – 0.165 s/km). The corresponding S-wave branches are found by multiplying both the τ and p values by the P/S-velocity ratio of 1.73. The S-waves are very clear in the p range 0.165 to 0.285 s/km where only S-waves can exist in this model. For slownesses below 0.1 s/km the S-waves gradually disappear because the source does not generate vertically propagating S-waves. The most complex part of the figure is for the slowness range 0.125 to 0.165 s/km for which the crust acts as a partial waveguide for P-waves (some P-wave energy will leak through the Moho when converted to S-waves at the free surface or at model discontinuities). The ray parameters bounding this interval is also seen to be slownesses at which abrupt changes in the waveform occur (due to phase shifts in the reflection coefficients). The lower value ($0.125 = 1/8.0$) is determined by the P-velocity below the Moho and the upper value ($0.165 \approx 1/6.1$) by the P-velocity near the surface. A similar change in waveforms is seen in the Moho reflected S-wave at the ray parameter corresponding to the S-velocity below the Moho. The rather strong wave with an intercept time of about 12 sec and a slowness of about 0.10 s/km is the Moho P-to-S reflection. Its amplitude depends on the reflection coefficient which have a maximum for slownesses around 0.08 s/km. Similar P-to-S reflections are visible also for some internal reflectors in the crust. In addition to the phases discussed above some multiple P- and S-waves are seen below the 'pure' P- and S-branches. In the slowness interval 0.125 to 0.165 many of the phases are probably multiples of mixed (P-S) waves.

The $\tau - p$ transformed data for the perturbed model (Fig. 6) is quite messy as compared to Fig. 5 and not unexpected when comparing the two datasets in the time-offset domain. The part that is most easily recognized when compared to Fig. 5 is the post-critical P-reflections. Except from this only some parts of the pre-critical S-reflections and possibly the Moho reflected P-phase is reasonably intact. All other phases are wiped out by interfering and scattered wavelets.

5. τ -sum inversion

Fortunately, the post-critical P-reflections that are most suitable to invert for the velocity depth model is also the part of the $\tau - p$ data that is best preserved when introducing model perturbations. The digitized parts of the 'principal branch' is shown in Fig. 7 for both models. The results are surprisingly consistent considering the otherwise remarkable differences in the two data sets. There might be some ambiguity in choosing which cycle to sample but in this case the same cycle appears to have been chosen for both models. The resolution is limited by the signal bandwidth. In real wide-angle reflection/refraction profiling work signals are recorded up to much higher frequencies (say 10–20 Hz) than those used in our synthetic experiments. However, with the rather high degree of scattering usually observed in continental crystalline crust at high frequencies, the effective frequency range (limited by the spatial correlation) is not much different from that used here.

The digitized $\tau - p$ curves were inverted to velocity-depth functions by means of the $\tau - \text{sum}$ method (Diebold and Stoffa, 1981). Here, a constant velocity layer is assigned to every sample of the $\tau - p$ curve. By dense $\tau - p$ sampling one can achieve an almost continuous velocity-depth function. It is not necessary to know if any part of the curve represent reflections or diving waves in a gradient layer. If there is some 'noise' in the sampled curve, artifacts like negative layer thicknesses may occur, but will not severely corrupt the end results. The inherent assumption of no low velocity zones in the model is no problem in our experiment. The resulting velocity-depth function for both models and the original input model is shown in Fig. 8. The general trend of the model is well recovered for both the perturbed and unperturbed dataset. None of the two recovered models is significantly better than the other. In both cases the differences between the obtained model and the original is less than 0.3 km/s for almost all depths. For both models the obtained velocities are generally too low in the upper part of the crust (down to about 20 km). This might be a coincidence, but probably reflect difficulties in sampling the $\tau - p$ curve at small intercept times (see Figs. 5 and 6).

6. Conclusions

Although most features of the $\tau - p$ transformed data for the unperturbed model was lost for the perturbed model, we were able to use the post-critical reflections in a $\tau - \text{sum}$ inversion to recover for both models, with about the same accuracy, the essential features of the original velocity-depth distribution. Further, for both models the finer details of the layering is lost and the resolution of the obtained velocity-depth functions seems to be about 0.2 km/s. The resolution is limited by the usable signal bandwidth which again depend on the degree of scattering. In our experiment the dominating frequency of the signal was about 2.5 Hz and the RMS of the perturbed medium was 3% for a von Kármán correlation function of order 0.3. Velocity-depth models obtained by $\tau - p$ transformation and $\tau - \text{sum}$ inversion seems to give a good laterally averaged velocity in the presence of velocity heterogeneities of the size used in this experiment, i.e., about 10 km, and recording offsets up to about 300 km.

Acknowledgements

This work was supported by the Air Force Office of Scientific Research, USAF under Grants F49620-92-J-0510 (B.O.R.) and F49620-94-1-0278 (E.S.H.).

References

Charette, E.E., 1991. *Elastic wave scattering in laterally inhomogeneous media*, Ph.D. thesis, MIT, Cambridge, Ma, USA, 222 pp.

Diebold, J.B. and Stoffa, P.L., 1981. The travelttime equation, tau-p mapping, and inversion of common midpoint data, *Geophysics*, **46**, 238-254.

Frankel, A. and Clayton, R.W., 1986. Finite difference simulations of seismic scattering: Implications for the propagation of short-period seismic waves in the crust and models of crustal heterogeneity, *J. Geophys. Res.*, **91**, 6465-6489.

Hestholm, S.O., Husebye, E.S. and Ruud, B.O., 1994. Seismic wave propagation in complex crust - upper mantle media using 2D finite difference synthetics, *Geophys. J. Int.*, **118**, 643-670.

Holliger, K. and Levander, A.R., 1992. A stochastic view of lower crustal fabric based on evidence from the Ivrea Zone. *Geophys. Res. Lett.*, **19**, 1153-1156.

Sguazzero, P., Kindelan, M., and Kamel, A., 1989. Dispersion-Bounded Numerical Integration of the Elastodynamic Equations, *Proceedings of the ICOSAHOM Conference, Como, Italy, June, 1989*, pp. 165-172. North Holland Publishing Company, The Netherlands.

Stoffa, P.L., Buhl, P., Diebold, J.B., and Wenzel, F., 1981. Direct mapping of seismic data to the domain of intercept time and ray parameter - A plane-wave decomposition, *Geophysics*, **46**, 255-267.

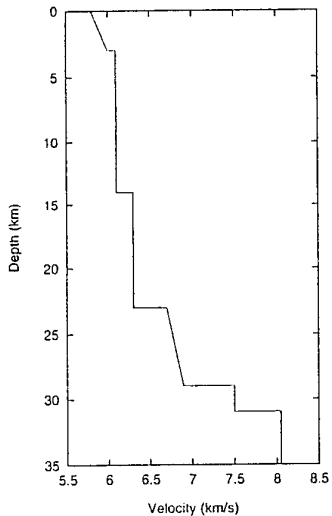


Figure 1. The P-velocity of the unperturbed model. The Moho is at 31 km. The same velocity-depth function was used as a basis for the perturbed model (Fig. 2).

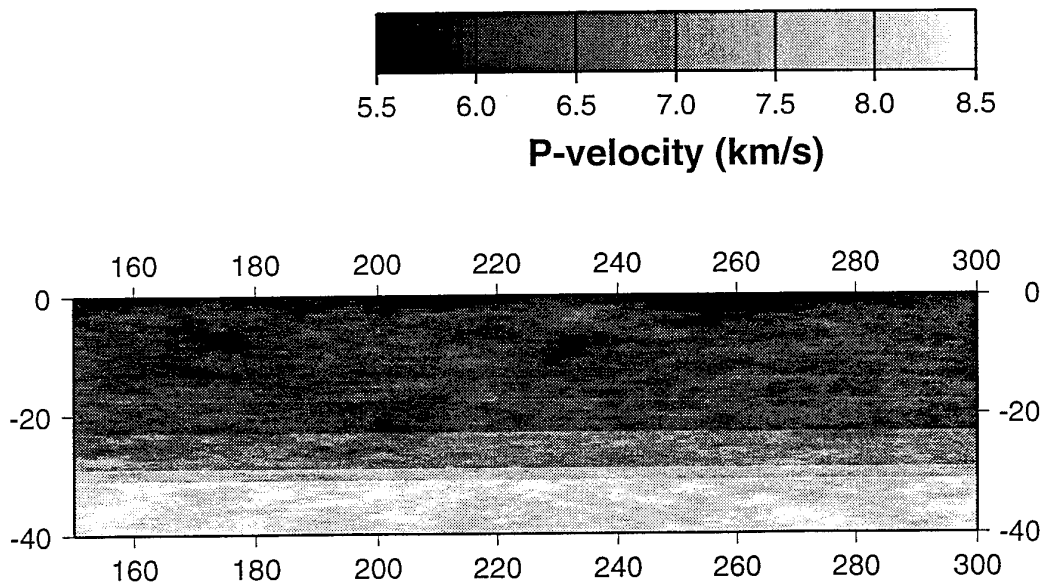


Figure 2. A section showing the P-velocities of the perturbed model. The (horizontally) averaged velocities are the same as for the unperturbed model (Fig. 1). The 2D auto-correlation function of the velocity perturbation field is a von Kármán function of order 0.3, horizontal and vertical correlation distances of 10 km and 2.5 km respectively, and an RMS of 3%.

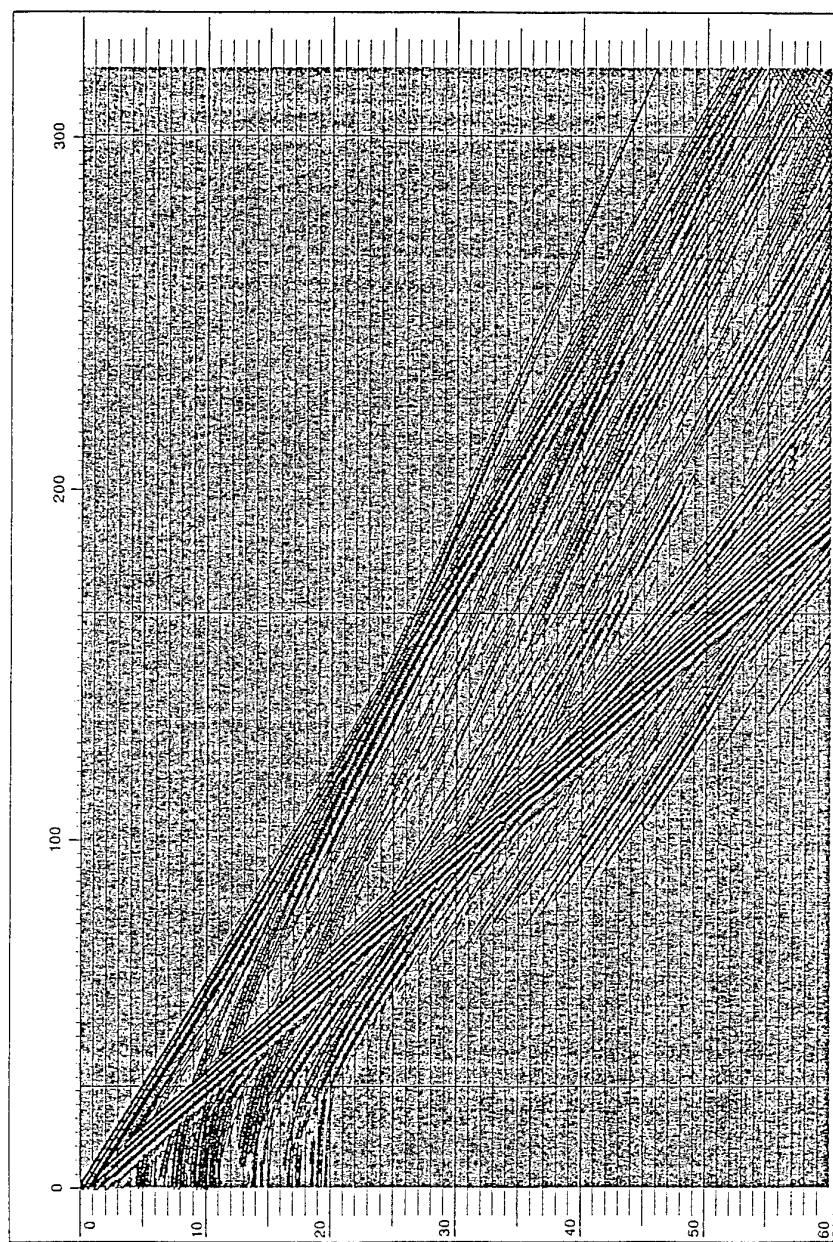


Figure 3. The time-offset section generated from the unperturbed model. Maximum offset (horizontal axis) is 320 km. Time (vertical axis) in seconds. The amplitude scaling is constant for the whole section.

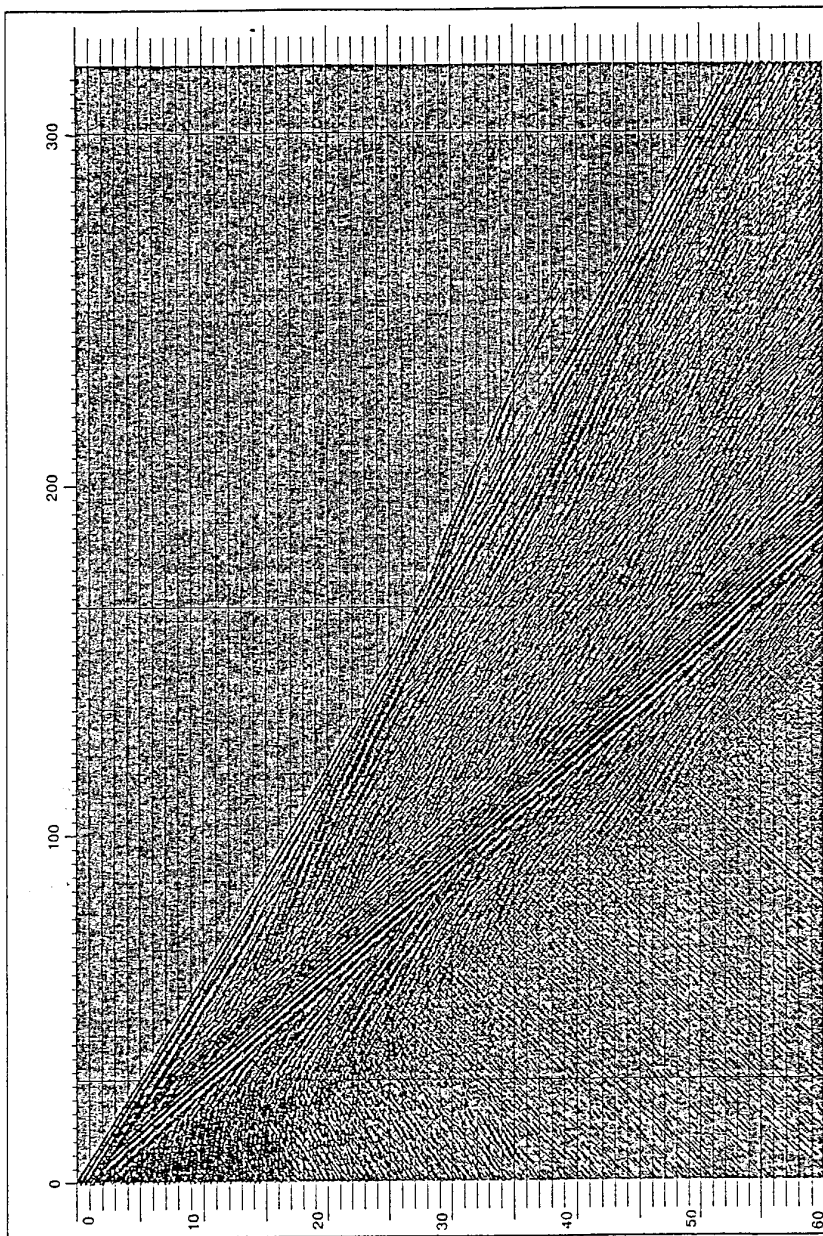


Figure 4. The time-offset section generated from the perturbed model. Maximum offset (horizontal axis) is 320 km. Time (vertical axis) in seconds. The amplitude scaling is constant for the whole section.

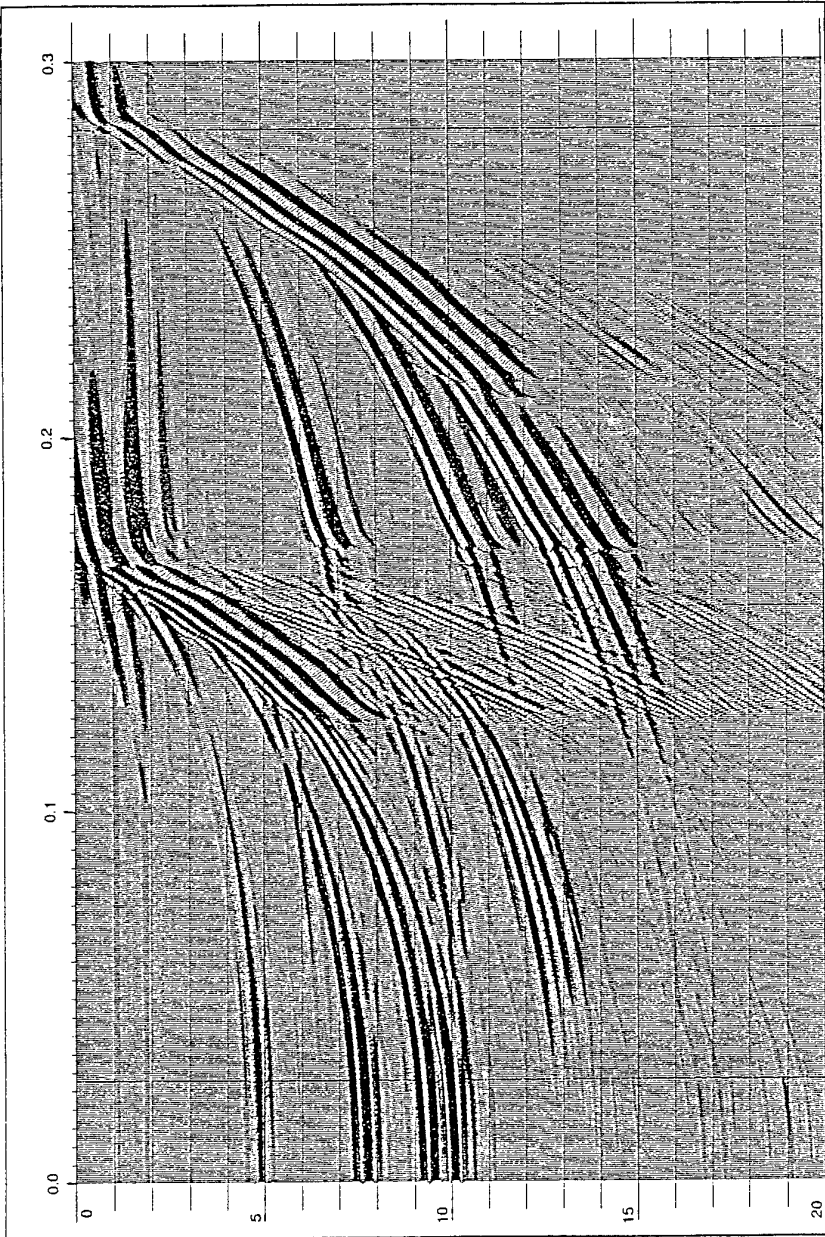


Figure 5. The $\tau - p$ transformed data from the unperturbed model. Slowness p along horizontal axis in s/km . Intercept time τ along vertical axis in seconds. See text for explanation of the different branches.

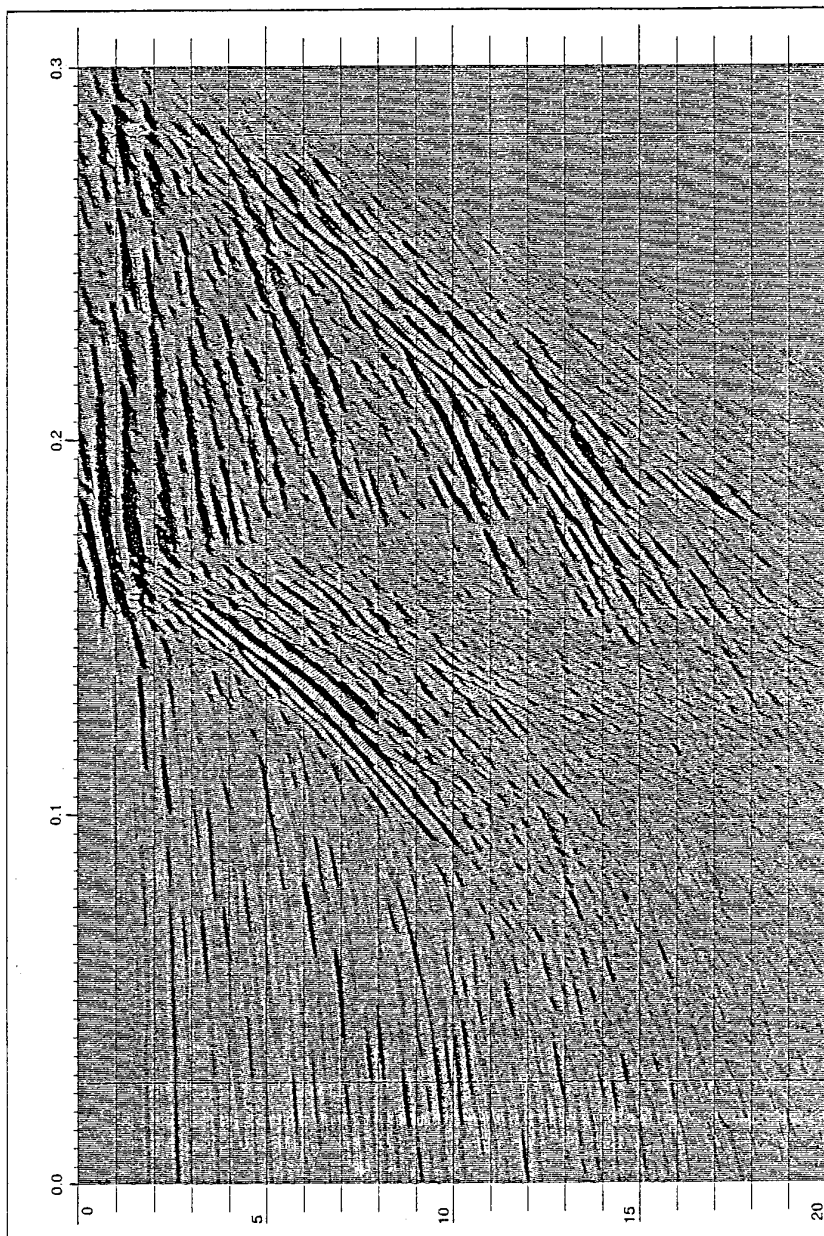


Figure 6. The $\tau - p$ transformed data from the perturbed model. Slowness p along horizontal axis in s/km. Intercept time τ along vertical axis in seconds.

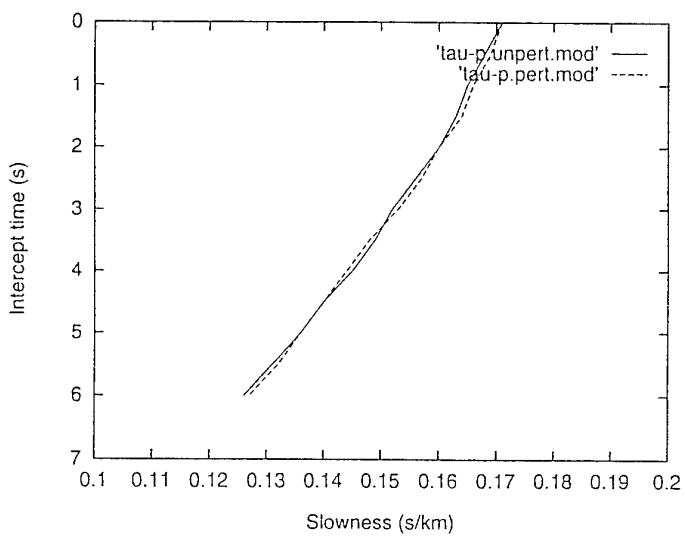


Figure 7. The 'principal branch' of the $\tau - p$ transformed data digitized from Figs. 5 and 6.

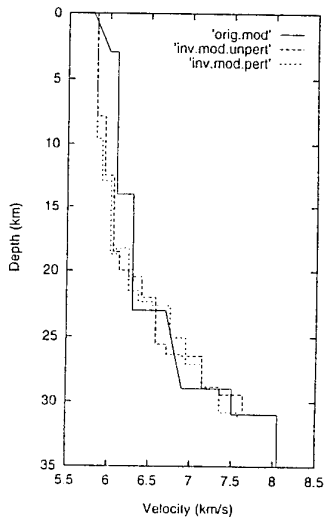


Figure 8. The velocity-depth functions obtained by τ -sum inversion of the $\tau - p$ curves shown in Fig. 7. For comparison the original model is also included.

Appendix D

ANNALI DI GEOFISICA, VOL. XXXVII, N. 3, June 1994

Near real time estimation of magnitudes and moments for local seismic events

Cenk Deniz Mendi ⁽¹⁾⁽²⁾ and Eystein S. Husebye ⁽¹⁾

⁽¹⁾ University of Bergen, Institute of Solid Earth Sciences, Bergen, Norway

⁽²⁾ On leave from TÜBİTAK, Marmara Research Center, Earth Sciences Department, Gebze, Kocaeli, Turkey

Abstract

The general popularity of magnitude as a convenient and robust measure of earthquake size makes it tempting to examine whether this parameter can be reliably estimated in near real time. In this study we demonstrate that this is indeed the case conditioned on the design of the signal detector being of STA/LTA type where STA is a short term signal power or rms estimate. Using real data we demonstrate the Random Vibration Theory relation that $A_{\max} \sim (2\ln N)^{1/2} A_{\text{rms}}$ is valid for non-stationary seismic signals. Using Rayleigh's theorem we also established a relation between A_{rms} and the flat portion of the source spectra. These A_{\max} and A_{rms} estimation procedures are used for determining conventional magnitudes and moment magnitudes for 29 events as recorded by the Norwegian Seismograph Network (NSN). We used here a procedure outlined by Sereno *et al.* (1988) and also their geometrical spreading and attenuation parameters derived from analysis of NORSAR recordings. Our magnitude and moment magnitude estimates for 5 different frequency bands are in good agreement with the M_L estimates derived from the conventional magnitude formulas in combination with empirical correction tables. Surprisingly, the A_{\max} and A_{rms} magnitudes produced consistent negative biased by ca. 0.4 units estimates even in the extreme 4-8 Hz band. In view of the good agreement between various types of magnitude estimates, we constructed conventional magnitude correction tables spreading and attenuation parameters from Sereno *et al.* (1988) for a variety of signal frequency bands. Near real time A_{\max} ad/or A_{rms} or correspondingly event magnitudes would be of significance in automatic phase association analysis, bulletin production for local and regional seismic networks and the earthquakes monitoring performances of such networks.

Key words random vibration theory - distance corrections - spreading and attenuation effects - network monitoring - capabilities in real time

1. Introduction

The concept of earthquake magnitude was firstly introduced by Richter (1935). He proposed a logarithmic amplitude scale tied to the first arriving P wave as a measure for the relative size of local Southern California earthquakes. This simple and robust magnitude scale being popular with

seismologists around the world, it has been extended to all distance ranges and many seismic phases (Nuttli, 1973; Båth *et al.*, 1981; Ebel, 1982). Despite the diversity of record measurements, tied to the maximum amplitudes of P , S and surface waves, all such scales are of similar forms

$$M = \log \left(\frac{A}{T} \right) + q(r, f) + c \quad (1.1)$$

where M is the magnitude, A the maximum phase amplitude, T is the period (s), q ac-

counts for geometrical spreading and attenuation as a function of distance r (km) and signal frequency (f) while c is a station correction term. Focal depth (h) is seldom included explicitly in magnitude formulas although it is significant in case of surface waves from deep events.

Although an occurring earthquake is a complex phenomenon, the Richter magnitude remains highly useful in many seismological contexts. A drawback with such measurement using conventional instrumentation is that earthquake phase amplitudes may be measured at frequencies beyond the corner frequency of the source spectra which cause a consistent magnitude bias. Therefore, many seismologists argue in favour of replacing magnitude with Aki's (1967) earthquake moment M_0 which may be obtained from inversion of broadband waveform data (Dziewonski and Gilbert, 1974; Jost and Herrmann, 1989) or equivalently the level of the flat portion of the source spectra. To avoid confusion, moment-magnitude scales have been introduced in the form of linear relationships between the moment (M_0) and magnitude. For example, Sereno *et al.* (1988) introduced the following formula for local Scandinavian earthquakes:

$$\log(M_0) = 1.03M_L + 17.1 \quad (1.2)$$

where M_L is the local L_g magnitude.

In eq. (1.1) the A/T measurement remains essentially a manual operation while the q -term is derived from empirical tables when an epicenter solution is at the hand. In this paper we address the problem of undertaking in near real time event magnitude and/or moment measurements. This study is tied to analysis of local events because M_L -magnitude estimation is often problematic due to complex geometrical spreading and attenuation relationships at small distance ranges. It is considered an important task in view of the widespread use of event magnitude in observational seismology and the potential of using amplitude information in automatic schemes

for epicenter location (Ruud *et al.*, 1993; Sambridge and Gallagher, 1993) and network performance simulations (Sereno *et al.*, 1988).

2. On line A/T estimation

Obviously for near real time magnitude/moment estimation, the A/T term must be an integral part of the signal detector design. The most popular ones in use are the so-called sliding window STA/LTA type which is a comparison of short and long term trace amplitude (a_i) averages (e.g., Ruud and Husebye, 1992). Common STA definitions are of the forms:

$$\text{STA (abs)} = \frac{1}{n} \sum_{i=1}^n |a_i| \quad (2.1)$$

$$\text{STA (rms)} = \left[\frac{1}{n} \sum_{i=1}^n a_i^2 \right]^{1/2} \quad (2.2)$$

Equivalent expressions are valid for LTA when the effective window length n is increased 10-20 times that of the STA window length. The STA and LTA terms are commonly measured in near real time on bandpass filtered seismometer output traces. When the STA/LTA ratio exceeds a present threshold, the presence of a seismic signal is declared. Our preference is for the rms related STA-LTA definitions also because signal rms is related to the signal power spectrum via the Parseval's theorem.

From eq. (2.2) the task is to estimate peak time domain amplitudes for the first arrival of P -waves or the dominant L_g -phase in case of local events that is the A/T -term in eq. (1.1). From the Random Vibration Theory (RVT) results of Cartwright and Longuet-Higgins (1956) we have the relation

$$E(A_{\max}) = A_{\text{rms}} f(N) \quad (2.3)$$

where E is expectation, N is the number of

extremes (peaks and troughs) and A_{rms} is the rms value of the signal. In the case of STA trace window, $A_{\text{rms}} = \text{STA}(\text{rms})$. We have for $f(N)$

$$f(N) = (2\ln N)^{1/2} \quad (2.4)$$

The RVT assumes stationary time series (Crandal and Mark, 1963) which are seldom the case for seismic recordings. However, Boore (1983) and Boore and Joyner (1984) have demonstrated that the RVT relation in eq. (2.3) performs well even in cases of peak signal accelerations and velocities as determined from time domain simulations. The validity of the simple linear relationship in eq. (2.3) was confirmed by extensive analysis of real data, and such results are detailed in the data analysis section.

Whether we prefer to measure magnitude (M_L) or moment (M_0), the A_{max} term is estimated from bandpass filtered traces, and thus must be corrected for the instrument response. A reasonable assumption here is that the displacement response spectra are approximately flat within the filter passband, and that the instrument response correction is tied to the center frequency of the bandpass filter. Similarly, the period (T) of the maximum signal amplitude is also tied to the center frequency of the bandpass filter. Thus, both the A_{max} and T terms in magnitude formula (eq. (1.1)) are obtained via eq. (2.3).

3. Magnitude measurements

The A/T -term derived via the detector parameter STA(rms) is sufficient for event magnitude estimation given that a tabulation of the distance dependent q -term in eq. (1.1) is available. However, for many regions the q -term is not well known at local and regional distances making corresponding event magnitude estimates unreliable. For example, as a rule the ISC does not estimate P -wave magnitudes for $r < 20^\circ$. In other cases, available correction ta-

bles were derived from old analog recordings in the 1-2 Hz bandpass while modern instrument recordings of local events are dominated by 3-6 Hz signal frequencies. An additional problem is that intraplate seismicity levels are so low that it is difficult to calibrate the local event magnitudes towards those obtained from teleseismic recordings.

In other words, local magnitude scales may differ significantly from each other, so recently seismologists have been exploring the usefulness of event moment magnitude scales.

3.1. Moment measurements

As mentioned above, the q -term in eq. (1.1) is not always well established, and a way of circumventing this problem is to introduce specific estimates of the geometrical spreading and attenuation (Q) effects. Following Sereno *et al.* (1988), we write for the amplitude spectrum of displacement at epicenter distance r

$$|A(f, r)| = S(f)G(r, r_0) \exp\left[\frac{-\pi f r}{Q(f)}\right] \quad (3.1)$$

where f is frequency, $S(f)$ source spectra, $G(r, r_0)$ geometrical spreading function with a reference distance (r_0), and $Q(f)$ the attenuation function. The attenuation function is of the form

$$Q(f) = Q_0 f^\gamma \quad (3.2)$$

where the frequency dependence is through the f^γ expression. The geometrical spreading term is of the form

$$G(r, r_0) = \begin{cases} (1/r)^\mu & ; r \leq r_0 \\ (1/r_0)(r_0/r)^\nu & ; r \geq r_0 \end{cases} \quad (3.3)$$

where the r_0 , μ , and ν parameters depend on the phase type and besides may vary from one tectonic regime to another. At lo-

cal distances the dominant signal in the records is the L_g -phase whose source spectrum in case of an earthquake is expressed as (Sereno *et al.*, 1989)

$$S(f) = S_0 H(f, f_c) \quad (3.4)$$

$$H(f, f_c) = \\ = \left(1 + (1 - 2B) \left(\frac{f}{f_c} \right)^2 + B^2 \left(\frac{f}{f_c} \right)^4 \right)^{-1/2} \quad (3.5)$$

where S_0 is the low frequency spectral source level, f_c is the corner frequency of the source spectrum, B is the amount of overshoot (Xie, 1993). We have the following relations for f_c and S_0 regarding M_0 :

$$f_c = c S_0^{-1/3}; \quad S_0 = \frac{M_0}{4\pi\varrho\beta^3} \quad (3.6)$$

where β is the crustal shear wave velocity, ϱ the crustal density and c a scaling constant. For moment/magnitude estimation, we must establish a relationship between the amplitude spectrum of the displacement ($|A(f, r)|$) and the near «real-time» record parameters, A_{rms} or A_{max} , namely

$$|A(f_{0i}, r)| = \sqrt{\frac{\Delta T}{2\Delta f_i}} A_{\text{rms}}; \quad i = 1, \dots, 5 \quad (3.7)$$

$$|A(f_{0i}, r)| \approx \frac{1}{2\Delta f_i} A_{\text{max}}; \quad i = 1, \dots, 5 \quad (3.8)$$

where f_{0i} represents the center frequencies of the 5 bandpass filters used in data analysis, $|A(f_{0i}, r)|$ is the amplitude spectrum at frequency f_{0i} and distance r , ΔT is the window length in s and Δf_i is the bandwidth of the i^{th} filter. The derivations of eq. (3.7) and eq. (3.8) are detailed in Appendix.

The source spectrum decays with f^{-2} beyond the f_c due to the H function. From eq. (3.6) we can estimate the S_0 and f_c parameters. However, in practice the corner frequency is not well resolved, so our preference was to fix it at a «safe» value of 20 Hz which is also very close to the bandwidth of the signals used in analysis (sampling frequency = 50 Hz). Under this assumption, the $H(f, f_c)$ is negligible and combining eqs. (3.1), (3.6), (3.7) and (3.8) we get

$$\begin{aligned} \log M_{0(\text{max})} &\approx \\ &\approx \log A_{\text{max}} - \log 2\Delta f_i + \log 4\pi\varrho\beta^3 + \\ &\quad - \log G(r, r_0) + \frac{\pi f t}{Q(f)} \log e \quad (3.9) \end{aligned}$$

$$\begin{aligned} \log M_{0(\text{rms})} &= \\ &= \log A_{\text{rms}} + \frac{1}{2} \log \frac{\Delta T}{2\Delta f_i} + \log 4\pi\varrho\beta^3 + \\ &\quad - \log G(r, r_0) + \frac{\pi f t}{Q(f)} \log e \quad (3.10) \end{aligned}$$

Note that P , S and L_g -phases from explosions and earthquakes respectively have different source representations. However, the main point is that it should be feasible to estimate in near real time event magnitude and event moment from «real-time» available signal detector parameters. The validity of this statement will be demonstrated in the next section.

4. Data analysis and results

In this section we would demonstrate that the deduced $A_{\text{max}} - A_{\text{rms}}$ relationship in eq. (2.3) appears to be valid for the recordings of local earthquakes and explosions at stations equipped with short period seismometers. We use observations from the Norwegian Seismograph Network (NSN) whose station locations are shown in fig. 1. A more subtle but extensive test was performed by calculat-

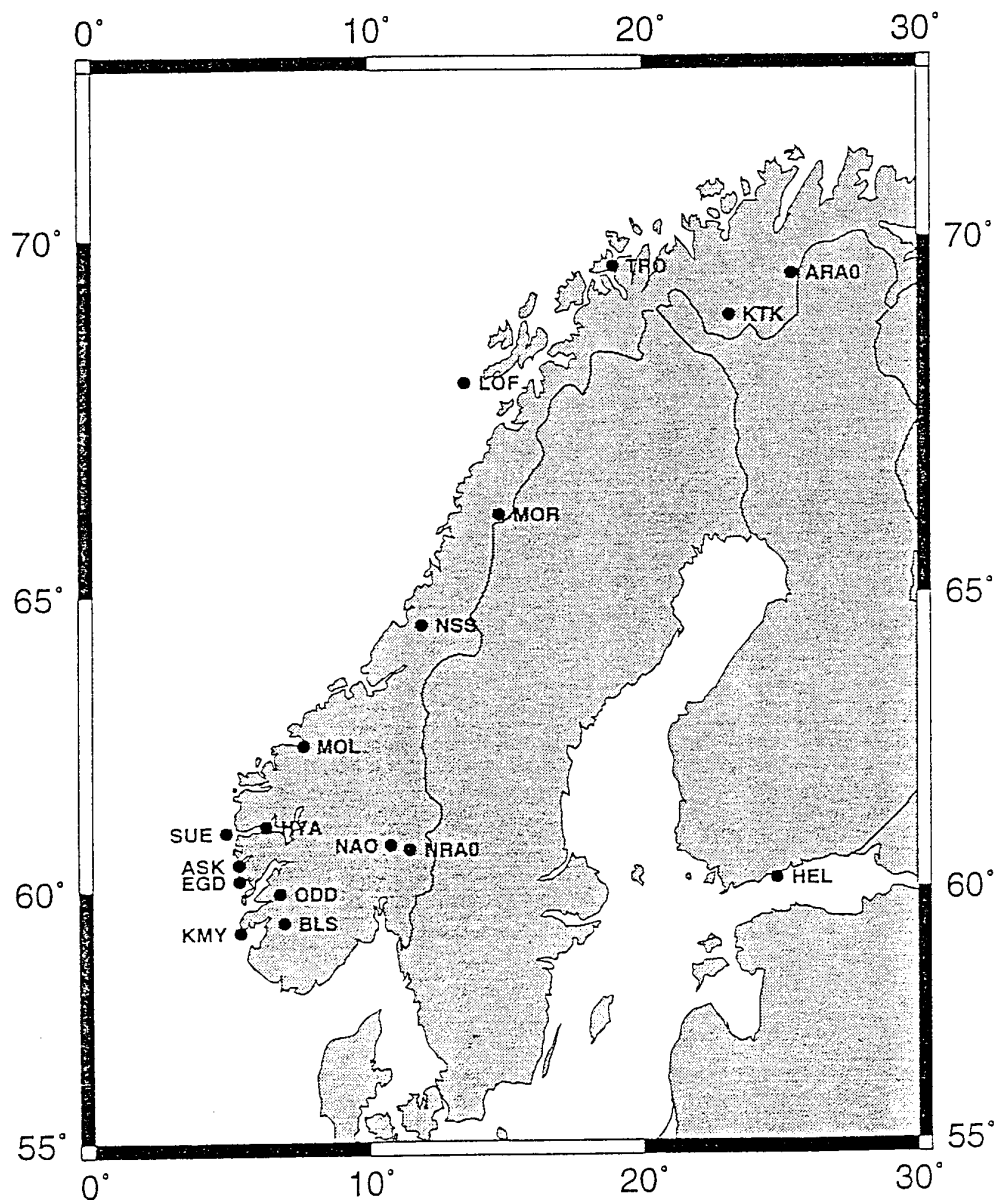


Fig. 1. Stations constituting the Norwegian Seismograph Network (NSN) which is operated by the University of Bergen. Some of the stations are equipped with three-component instrumentation. In our analysis only the vertical short period recordings are used. The NORSAR operated regional arrays NORESS (NAO, NRA0) and ARCESS (ARA0) are also marked.

Table I. Listing of all the events used in our analysis. The focal parameters are taken from the monthly bulletins for the Norwegian Seismic Network (NSN) as published by the University of Bergen. The M_c and M_L notations reflect NSN coda wave magnitude and NORSAR reported M_L (L_g -waves) magnitude, respectively. We have introduced a few modifications in parameter listing; all presumed explosions (EXP) are given zero focal depth. The separation of events into EXP and EQ (earthquake) populations are not based on specific classification criteria. Potential errors here would not significantly change our analysis results.

N.	Date		Time		Location		M_c	M_L	H (km)	# Stat.	Source type
	(d/m/y)	(h:min:s)	(LatN)	(LonE)							
1	26/08/93	10.34:32.0	59.05	5.77	2.6	2.2	0	8	0	8	EXP
2	26/08/93	19.22:04.9	61.11	4.07	2.8	2.5	18	8	0	8	EQ
3	10/09/93	13.11:23.8	58.34	6.36	2.7	2.0	0	5	0	5	EXP
4	13/09/93	05.25:14.4	66.34	5.67	3.9	3.2	11	10	0	10	EQ
5	15/09/93	09.58:38.1	60.60	4.79	2.1	1.6	0	7	0	7	EXP
6	15/09/93	15.31:29.7	67.11	20.84	3.2	1.8	0	4	0	4	EXP
7	21/09/93	13.15:21.1	58.33	6.31	3.0	2.5	0	7	0	7	EXP
8	28/09/93	16.44:53.9	58.49	10.62	2.9	2.3	15	5	0	5	EQ
9	28/09/93	16.57:42.1	60.46	5.15	1.6	1.4	0	6	0	6	EXP
10	29/09/93	14.12:21.5	58.15	6.31	2.8	2.2	0	6	0	6	EXP
11	02/10/93	08.30:55.3	60.39	5.02	1.8	1.5	0	6	0	6	EXP
12	03/10/93	23.48:35.5	60.06	7.29	2.5	1.8	15	7	0	7	EQ
13	04/10/93	20.21:48.3	61.94	1.44	2.3	1.0	11	5	0	5	EQ
14	07/11/93	23.40:44.0	67.84	20.08	2.5	1.7	15	4	0	4	EQ
15	07/11/93	23.43:17.2	66.28	7.02	3.1	2.5	25	4	0	4	EQ
16	08/11/93	14.28:17.3	59.91	2.72	2.4	1.5	15	7	0	7	EQ
17	12/11/93	19.54:36.0	59.69	12.86	3.4	2.9	16	6	0	6	EQ
18	15/11/93	15.04:25.6	62.17	3.27	2.7	1.9	15	5	0	5	EQ
19	21/11/93	01.53:56.3	60.18	4.96	2.6	2.1	12	6	0	6	EQ
20	27/11/93	18.57:52.7	60.47	11.66	3.1	2.2	0	5	0	5	EXP
21	13/12/93	09.00:09.5	56.75	2.74	3.1	2.6	12	6	0	6	EQ
22	27/12/93	05.20:46.3	61.29	2.79	3.3	3.6	14	8	0	8	EQ
23	03/01/94	22.12:59.8	61.76	4.19	2.6	2.4	17	7	0	7	EQ
24	07/01/94	09.06:22.6	60.60	2.43	2.3	1.8	23	5	0	5	EQ
25	15/01/94	00.00:26.2	65.23	7.58	2.8	1.6	2	3	0	3	EQ
26	19/01/94	09.16:54.8	66.36	14.60	2.4	1.4	0	3	0	3	EXP
27	21/01/94	01.26:14.1	65.98	11.89	3.1	2.1	19	2	0	2	EQ
28	25/01/94	03.07:58.3	62.46	5.07	2.6	1.9	20	5	0	5	EQ
29	26/01/94	17.27:47.1	66.84	13.58	3.0	2.3	0	5	0	5	EXP

ing magnitudes and moments for the 29 events listed in table I using the approach detailed in the previous section.

4.1. A_{\max} deduced from A_{rms}

In figs. 2a-f to 4a-f the apparent validity of the A_{\max} - A_{rms} relationship is demonstrated for station KMY recording of Event 4 in table I. In (a) the P and L_g phase

recordings are shown; (b)-(c) the independently observed A_{\max} versus A_{rms} or STA for both P and L_g waves; (d)-(e) the corresponding number of extremes within the individual STA windows. Note that an extrem occurs when the second derivative of the trace time function is zero. For unfiltered traces, as in figs. (d) and (e), the number of extreme would be relatively high due to the ripples overlaying the signal trace. The linear A_{\max} - A_{rms} relationship in

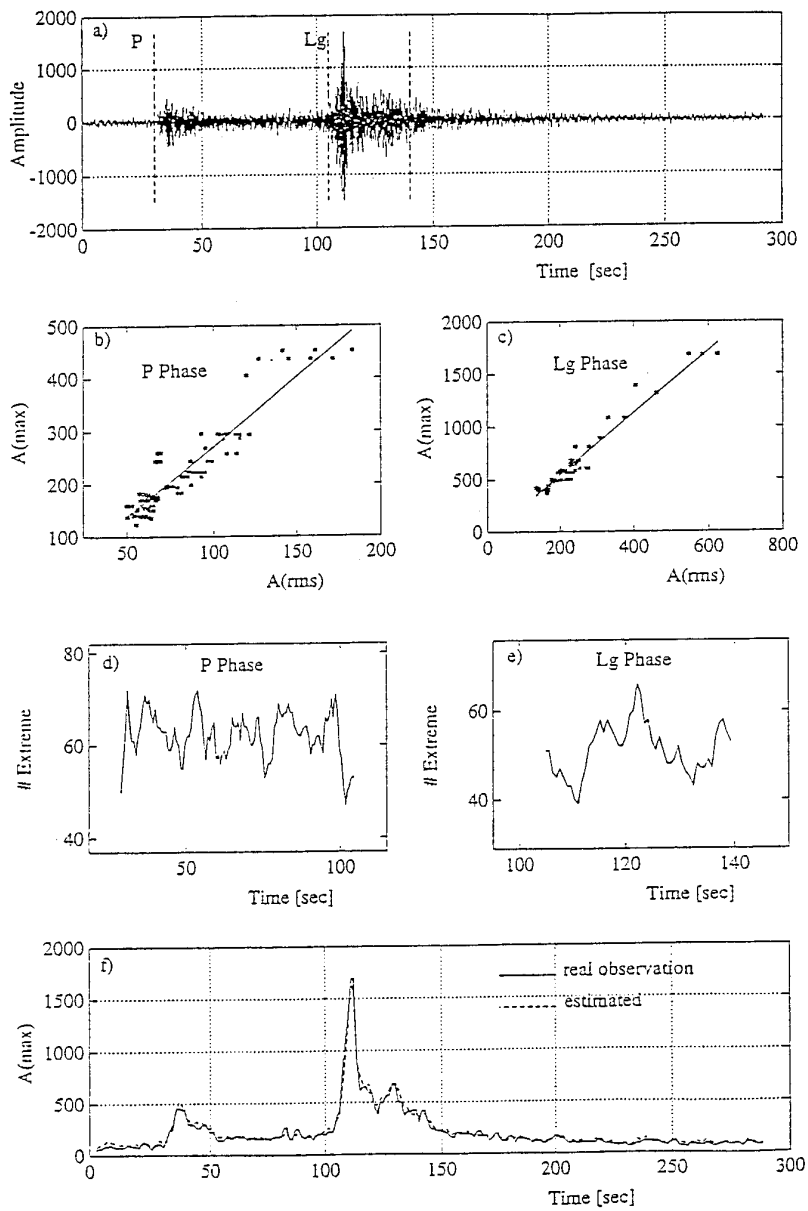


Fig. 2a-f. A_{\max} - A_{rms} analysis for KMY unfiltered recordings of Event 4 in table II at an epicentral distance of 795 km. a) Original vertical trace record; b) and c) A_{\max} versus A_{rms} for P- and L_g -phases respectively. The window length used in the evaluation of A_{rms} is 2.5 s; d) and e) number of extremes N for P- and L_g -phases; f) observed and estimated A_{\max} using eq. (2.3). The two curves match each other almost perfectly.

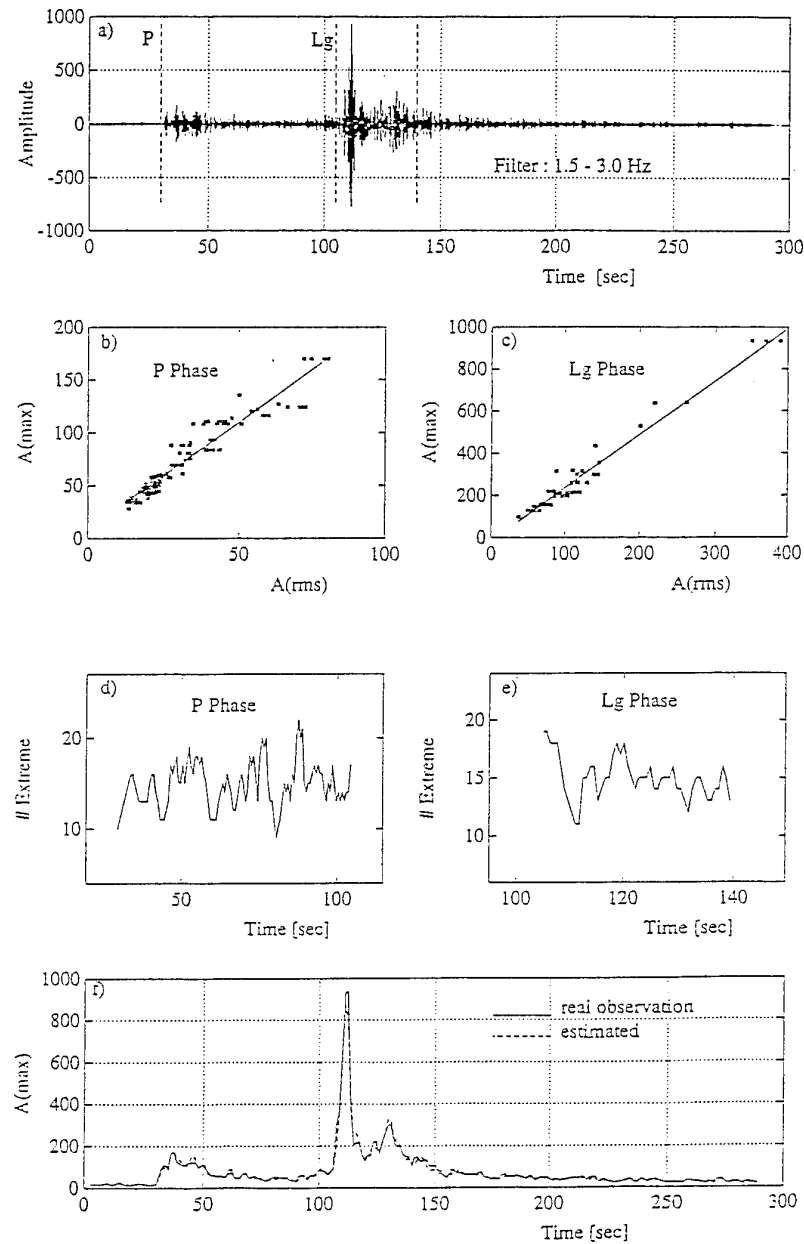


Fig. 3a-f. A_{\max} - A_{rms} analysis for KMY recordings in the 1.5-3.0 Hz passband of Event 4 in table II. Otherwise, caption as in fig. 2a-f.

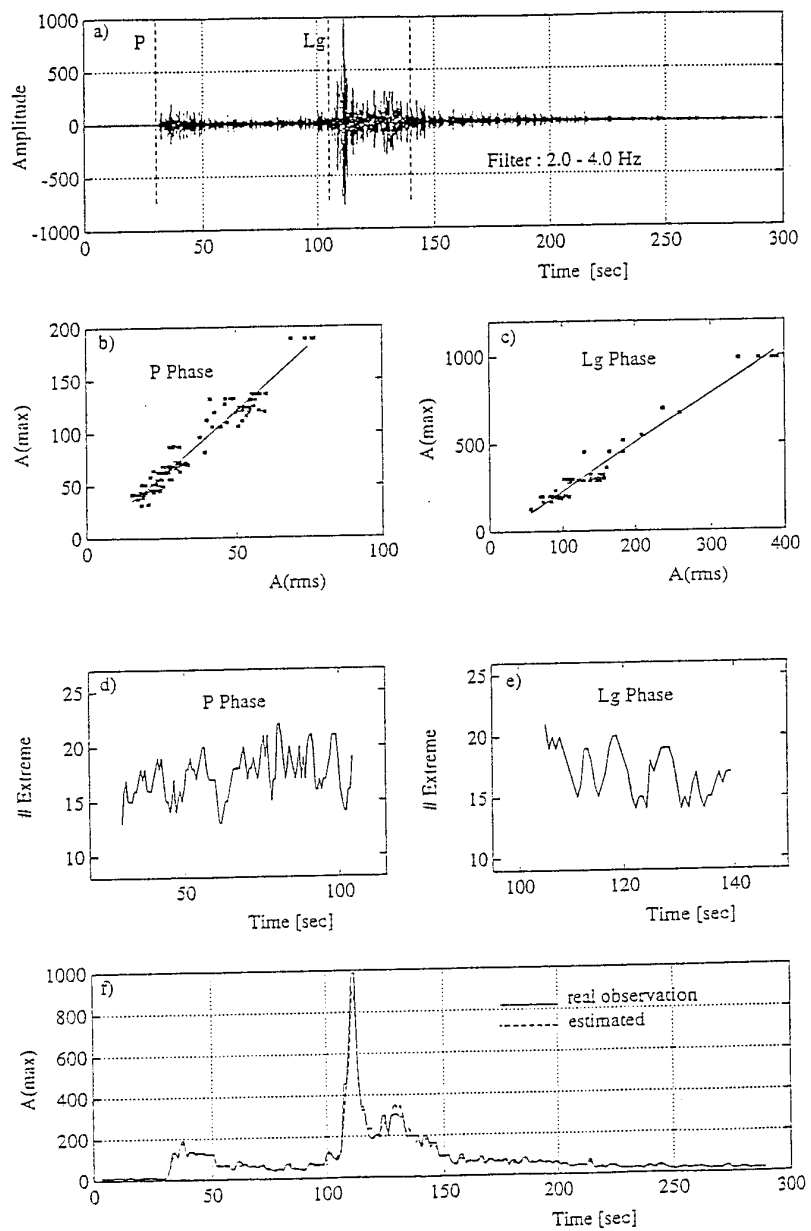


Fig. 4a-f. $A_{\text{max}}-A_{\text{rms}}$ analysis for KMY recordings in the 2.0-4.0 Hz passband of Event 4 in table II.
Otherwise, caption as in fig. 2a-f.

figs. (b) and (c) can be predicted from the number of extremes (N) in figs. (d) and (e); the agreement is very good. From this result we expect an excellent agreement between observed and estimated A_{\max} values which indeed is the case from results presented in figs. (f). Even in the extreme cases of very peaked L_g -waves, this agreement remains good.

So far, we have computed the N -parameter for every STA window: since this parameter fluctuates moderately within a specific filter band and the $(2\ln N)^{1/2}$ expression of eq. (2.3) vary slowly with N , there is really no need to update the N -estimates for every STA window. Anyway, the essence of the results presented in figs. 2a-f to 4a-f is that the STA values as estimated in near real-time for a rms type of STA/LTA detector can be used for accurately estimating the maximum trace amplitudes for any part of the short period seismometer records.

4.2. Magnitude estimation

Given the epicentral distance and A_{\max} or A_{rms} , we can compute event magnitudes or event moments as detailed above. This was done for the 29 events listed in table I and then these moments were converted to event magnitudes using the conversion formulas and the parameter values given in table III. These moment magnitudes are denoted $ML(\text{Ser})_{\max}$ and $ML(\text{Ser})_{\text{rms}}$. Since frequency dependence on M_L -estimates is a debated topic, we computed $ML(\text{Ser})$ for 5 frequency bands as indicated in table II. Using the maximum amplitude values for S or L_g -phases we also computed conventional event magnitudes using various types of correction curves (spreading and attenuation) as taken from NORSAR, Alsaker *et al.* (1991), and the Seismological Observatory in Helsinki (details also in table III). In the latter cases, there is hardly any frequency dependence in the distance correction term, so here only the $f2$ (1.5-3 Hz) frequency band was used in the magnitude calculations.

In table II all magnitude values represent averages with respect to the number of reporting stations listed in table I. The obtained event magnitudes are similar at the lower frequencies, irrespective of epicenter distance. The only exception here is the ML_H which are consistently high by ca. 0.6 magnitude units. A comparison with the coda magnitudes (M_c) gives that these are also consistently high and besides appear to be less stable than the NORSAR reference magnitudes (M_L). The latter are in reasonable agreement with the $f2$ $ML(\text{Ser})$ values in table II that are consistently low by ca. 0.3 magnitude units. These features are illustrated in fig. 5a,b showing plots of $ML(\text{Ser})_{\max}$ versus M_L -magnitudes reported by NORSAR.

Frequency dependence of the magnitude estimates is obvious from the table II results, but there is hardly any difference between the $ML(\text{Ser})_{\text{rms}}$ and $ML(\text{Ser})_{\max}$ estimates. The attenuation parameter may be important in this respect, so we recalculated the $ML(\text{Ser})$ magnitudes for $\gamma = 0.20$ and $\gamma = 0.14$ equivalent to increased signal attenuation. Its effect is to increase the $f4$ and $f5$ magnitudes by only 0.1 magnitude units in average since epicenter distances are generally less than 250 km. On the other hand, the differences between $f1$ and $f2$ as compared to $f4$ and $f5$ magnitude estimates remain at ca. 0.4 magnitude units. In fig. 6a-f we have plotted event magnitudes for individual stations as a function of distance for $\gamma = 0.26$, $\gamma = 0.40$ and $\gamma = 0.55$ which are equivalent to decreasing attenuation. In these plots the average event magnitude is adjusted to a value of 2.5 units, while the stations at distances less than 250 km are deleted since the effect of frequency dependence is as mentioned very small for such ranges. From fig. 6a-f, we see that a γ value of 0.40 or 0.55 would be a better choice than $\gamma = 0.26$. These results contradicting those in table II, are not considered conclusive since we have few observations beyond 500 km and the scattering in the individual stations M_L values is of the order of some tens of a magnitude unit.

Table II. Magnitude estimates for the events listed in table I. f_1, f_2, f_3, f_4 and f_5 represent different frequency bands which are 1-2 Hz, 1.5-3 Hz, 2-4 Hz, 3-6 Hz and 4-8 Hz, respectively. Column M_L is L_g event magnitudes as reported by NORSAR using NORESS recordings while M_c is coda magnitude based NSN recordings as reported in the bulletin. $ML(Ser)_{max}$ is magnitude estimates tied to maximum amplitude observations (eq. (3.8)) while $ML(Ser)_{rms}$ are corresponding moment magnitude estimates tied to the rms values (eq. (3.7)). Common features are averaging over reporting stations (table I) and using Sereno *et al.* (1988) spreading and attenuation constants (table III). Columns ML_N , ML_A and ML_H are magnitude estimates similar to $ML(Ser)_{max}$ except that the distance correction terms used are those of NORSAR, Alsaker *et al.* (1991) and Helsinki (table III). Since these are frequency independent only magnitudes in the f_2 band are listed. Note the overall similarity of event magnitudes in the f_2 band with the exception of ML_H and M_c estimates. Another notable feature is the consistent decay in $ML(Ser)$ from the f_1-f_2 bands towards the f_4-f_5 bands. We take this to imply that the S/L_g excitation is less effective at higher signal frequencies.

N.	M_L	M_c	$ML(Ser)_{max}$					$ML(Ser)_{rms}$					ML_N ML_A ML_H		
			f_1	f_2	f_3	f_4	f_5	f_1	f_2	f_3	f_4	f_5	f_2	f_2	f_2
1	2.2	2.6	2.5	2.3	2.2	2.0	2.0	2.6	2.4	2.3	2.1	2.1	2.3	2.3	2.9
2	2.5	2.8	2.9	2.8	2.7	2.6	2.5	3.0	2.9	2.8	2.6	2.5	2.8	2.7	3.3
3	2.0	2.7	2.5	2.3	2.2	2.1	2.0	2.6	2.5	2.4	2.2	2.1	2.3	2.3	2.9
4	3.2	3.9	3.7	3.7	3.6	3.5	3.5	3.7	3.6	3.5	3.2	2.9	3.8	3.6	4.1
5	1.6	2.1	2.1	1.9	1.8	1.6	1.5	2.2	2.0	1.9	1.7	1.6	1.8	1.8	2.4
6	1.8	3.2	2.0	1.8	1.9	2.3	2.3	2.1	1.9	2.0	2.3	2.3	1.9	1.9	2.4
7	2.5	3.0	2.7	2.6	2.5	2.5	2.4	2.8	2.7	2.6	2.5	2.4	2.6	2.5	3.1
8	2.3	2.9	2.3	2.2	2.3	2.3	2.1	2.4	2.3	2.3	2.2	1.8	2.2	2.2	2.8
9	1.4	1.6	1.6	1.4	1.3	1.1	0.9	1.8	1.5	1.4	1.2	1.1	1.3	1.3	1.8
10	2.2	2.8	2.5	2.4	2.3	2.1	2.0	2.7	2.5	2.4	2.2	2.0	2.4	2.4	3.0
11	1.5	1.8	1.8	1.5	1.3	1.2	1.1	1.9	1.7	1.5	1.4	1.2	1.3	1.4	2.0
12	1.8	2.5	2.1	2.0	1.9	1.8	1.7	2.2	2.1	2.0	1.9	1.7	1.8	1.9	2.5
13	1.0	2.3	1.8	1.5	1.5	1.4	1.3	1.9	1.6	1.5	1.3	1.2	1.5	1.5	2.0
14	1.7	2.5	2.3	2.2	2.1	1.8	1.6	2.4	2.3	2.1	1.8	1.5	2.1	2.1	2.7
15	2.5	3.1	2.9	2.9	2.8	2.5	2.5	3.0	2.9	2.7	2.4	2.2	2.9	2.8	3.5
16	1.5	2.4	2.1	1.8	1.7	1.6	1.5	2.1	1.8	1.7	1.6	1.5	1.7	1.7	2.3
17	2.9	3.4	3.1	2.9	2.9	2.8	2.7	3.2	3.0	2.8	2.6	2.3	3.0	2.9	3.5
18	1.9	2.7	2.4	2.3	2.2	2.1	2.0	2.5	2.3	2.3	2.1	1.9	2.2	2.2	2.8
19	2.1	2.6	2.4	2.3	2.2	1.9	1.8	2.4	2.3	2.3	2.1	1.9	2.1	2.1	2.7
20	2.2	3.1	2.6	2.5	2.3	2.2	2.1	2.7	2.6	2.4	2.1	1.9	2.5	2.5	3.1
21	2.6	3.1	2.4	2.3	2.3	2.4	2.4	2.5	2.3	2.3	2.2	2.0	2.3	2.3	2.9
22	3.6	3.3	3.6	3.4	3.2	3.0	2.9	3.7	3.4	3.2	2.9	2.7	3.4	3.3	3.9
23	2.4	2.6	2.9	2.7	2.7	2.5	2.4	2.9	2.8	2.7	2.5	2.4	2.6	2.6	3.3
24	1.8	2.3	2.2	2.1	2.0	1.8	1.7	2.3	2.1	2.0	1.8	1.7	2.0	2.0	2.6
25	1.6	2.8	2.0	1.8	1.8	1.9	1.9	2.1	1.9	1.9	1.8	1.7	1.8	1.8	2.4
26	1.4	2.4	2.0	1.7	1.5	1.3	1.3	2.1	1.8	1.5	1.4	1.4	1.7	1.7	2.2
27	2.1	3.1	2.4	2.3	2.2	2.1	2.0	2.5	2.4	2.3	2.2	2.1	2.2	2.2	2.9
28	1.9	2.6	2.3	2.0	1.9	1.7	1.6	2.3	2.1	1.9	1.7	1.5	1.9	1.9	2.5
29	2.3	3.0	2.4	2.3	2.2	2.1	1.9	2.5	2.4	2.3	2.1	1.9	2.2	2.2	2.8

The above attenuation results signify the importance of path effects and station corrections, and also the observational fact that L_g -wave excitation is relatively less effective at signal frequencies above 3-4 Hz.

5. Discussion

In this study we have explored the possibility of estimating event magnitude in near real time. At this stage of development we have concentrated on demonstrating that

Table III. Listing of correction formulas as used for the estimated magnitudes tabulated in table II. M_0 = moment, A = peak amplitude in nm and Δ = epicentral distance in km. $F(\Delta, T)$ correction function is shown in fig. 7 for $T = 0.45$ s.

Magnitude formulations	Reference
$\log M_0 = 1.03 ML(\text{Ser}) - 17.1$ (EQ)	
$\log M_0 = 1.04 ML(\text{Ser}) - 17.7$ (EXP)	
$Q_0 = 560; \gamma = 0.26$	Sereno <i>et al.</i> (1989)
$r_0 = 100$ km; $\mu = 1; \nu = 1/2$	
$\varrho = 2.7$ gr/cm ³ ; $\beta = 3.5$ km/s	
$ML_N = \log (100 A) + F(\Delta, T)$	NORSAR
$ML_A = \log A + 0.91 \log \Delta + 0.00087 \Delta - 1.31$	Alsaker <i>et al.</i> (1991)
$ML_H = \log A + 1.27 \log \Delta - 1.44$	Helsinki Seismological Observatory

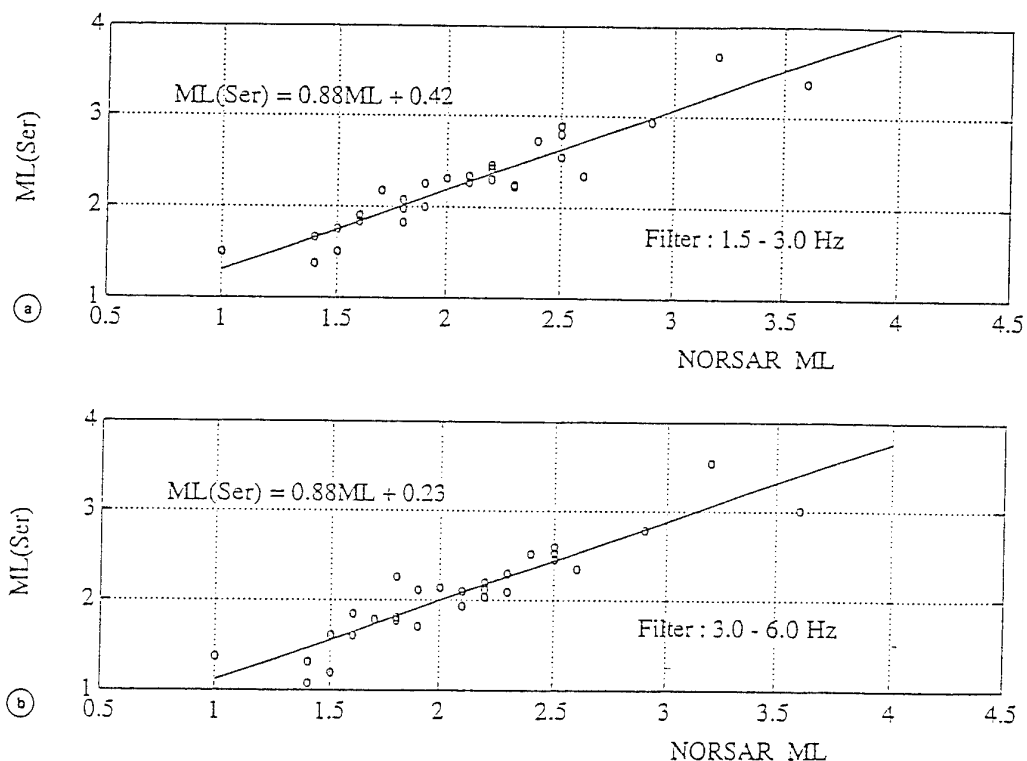


Fig. 5a,b. $ML(\text{Ser})_{\text{max}}$ magnitude estimates from table II versus the reference NORSAR M_L magnitude estimates in table II. The small offset may in part reflect local site effects since the NORESS array is located outside the NSN siting area.

A_{\max} and/or A_{rms} and hence event magnitudes can be obtained from signal detector outputs of the STA/LTA types. In figs. 2a-f, an excellent agreement between observed and estimated maximum amplitude in all frequency bands considered is demonstrated. However, we have not contemplated such maximum amplitude estimates in a real time operational environment since we are not directly involved in this kind of work.

Through the analysis of 29 events (earthquakes and explosions) we have determined A_{\max} and A_{rms} as described above for both conventional and moment magnitude estimates. In the former cases, we used empirical formulas for the geometrical spreading and attenuation effects taken from Alsaker *et al.* (1991) and those used at NORSAR and Helsinki in their bulletin works. In many regions such correction tables are not available, so we explored the possibility of using moment magnitudes based on spreading and attenuation parameters estimated directly from spectral analysis of local event records. All the various types of M_L estimates for local events recorded by the Norwegian Seismograph Network (NSN) stations proved to be mutually consistent. The only exception here was the ML Helsinki estimates which appeared to be positive biased by ca. 0.6 magnitude units. In the NSN monthly bulletins, coda magnitudes are routinely reported. These estimates also appear to be positive biased and somewhat unstable.

Initially, we allowed the corner frequency (f_c) to be a free parameter but for larger events $M_L > 3.0$, this caused erroneous estimates in the sense that unrealistic magnitudes estimates were obtained. The remedy here was to freeze the corner frequency at 20 Hz. This also implies that the estimate of the f_c parameter is not well constrained in the analysis procedure used. For larger events, say for $M_L > 4.5$, some of the frequency bands considered here would be beyond the corner frequency and hence the corresponding moment magnitude estimates should have negative biases. Indica-

tions of such cases would be negative differences between low and high frequency bands, actually observed for nearly all events used in analysis (table II). From the previous section, we rule out relatively strong signal attenuation or exceptionally low corner frequencies as a plausible explanation for these observational features. Instead, we consider that the S/L_g signal excitation spectra are not flat met to the corner frequency as presumed in our theoretical modelling. In other words, the most consistent and correct magnitude estimates are obtained for signal frequencies in 1-3 Hz range; at higher signal frequencies the observed negative biases can be computed by introducing frequency dependent station corrections if considered worth while.

A recent tendency in establishing local magnitude scales is the synthesis of the original Wood-Anderson seismograph recordings from Southern California (Richter, 1935) (e.g. Alsaker *et al.*, 1991). Our preference is for the moment magnitude estimation approach simply because of its anchoring on physical source representation and well established wave propagation parameters. These parameters can be obtained through analysis of appropriate signal spectra (Sereno *et al.*, 1988) which besides would be representative of the station/network siting area. In contrast, the wave propagation regime of Southern California is not representative for most of the network areas elsewhere and hence not well suited as a magnitude reference base. In a seismic hazard study for Southern Norway, Singh *et al.* (1990) discussed various magnitude formulas in use and also the associated attenuation parameters including those of Sereno *et al.* (1988). The differences here appear larger than the corresponding differences in estimated event magnitudes and a reconciling explanation here is that spreading and attenuation effects are not easily separated. The combined effects are incorporated in the magnitude correction curves. The relative consistency of $ML(\text{Ser})$ magnitudes (table II) implies that it should be possible to construct

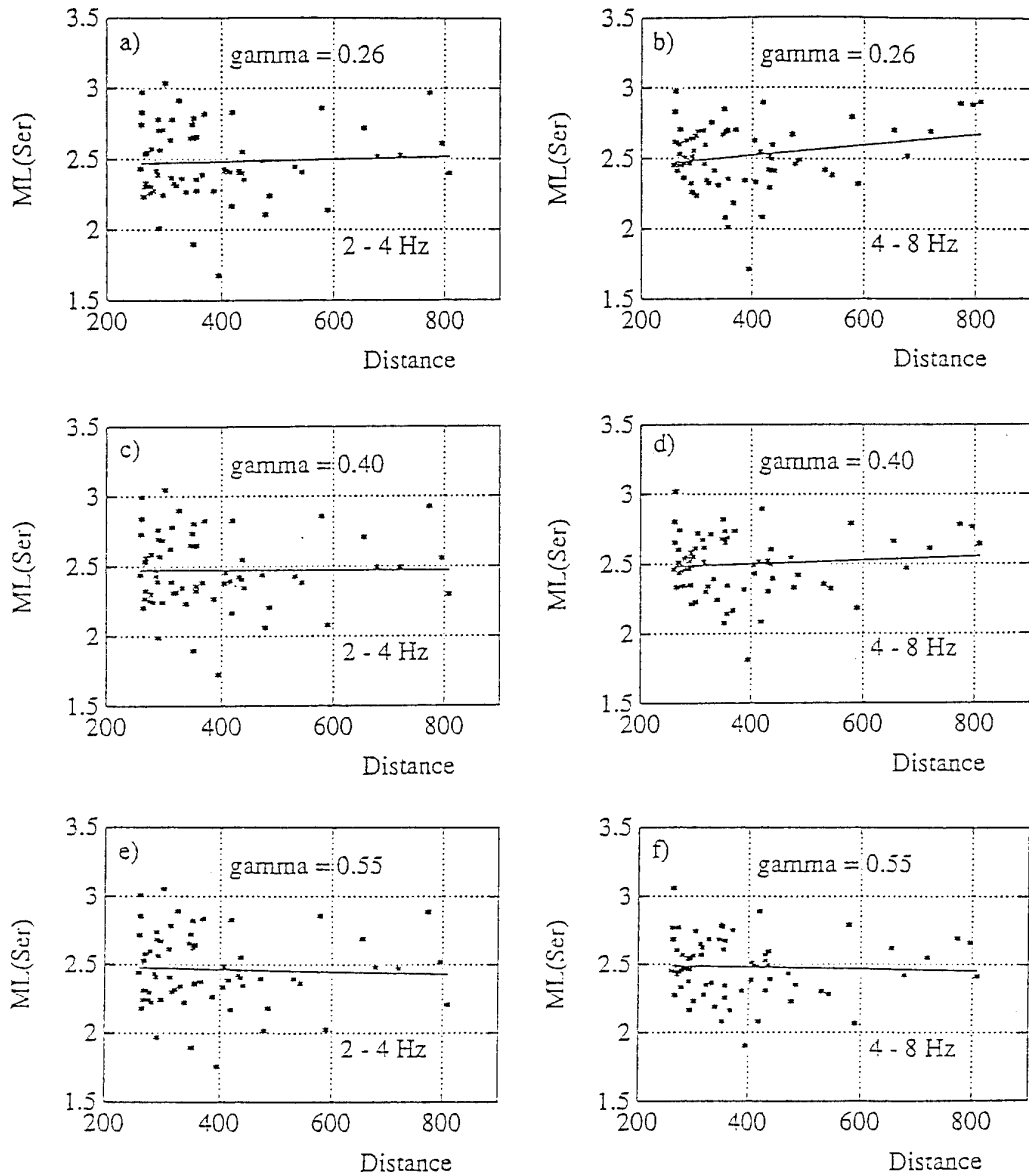


Fig. 6a-f. The $ML(Ser)$ estimates as a function of epicenter distance and different values of the attenuation parameter γ . The corresponding linear regression lines are also shown. Note that network $ML(Ser)_{max}$ average for each event is scaled to a reference magnitude of 2.5 units and this scaling constant would be different for each frequency band considered. Observations for distances below 250 km were excluded from the figure. There are very few observations beyond 500 km so it is not quite obvious that the best fitting $\gamma = 0.40$ (diminishing attenuation) is truly correct. The table II results give less differences between low and high frequency estimates for the decreasing γ values.

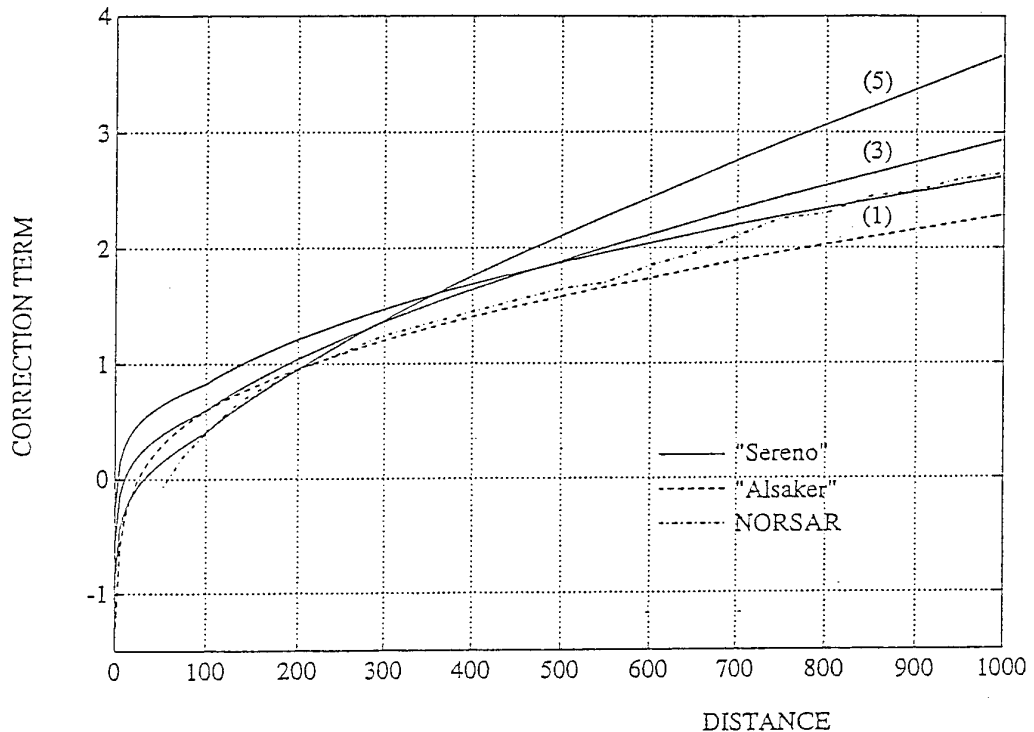


Fig. 7. Generating distance-correction curves from the Sereno *et al.* (1988) spreading and attenuation parameters as listed in table III. For comparison the corresponding Alsaker *et al.* (1991) and NORSAR ($T = 0.45$ s) curve are shown. The correction curves derived from Sereno *et al.* (1988) are plotted for the filters f_1 , f_3 and f_5 . In table II the $ML(Ser)$ and ML_A magnitude estimates are very similar which is also expected from fig. 7 since epicenter distances generally are less than 250 km. The NORSAR reported magnitudes (M_L column in table II) are in average 0.3 units lower than expected since the corresponding epicenter distances are in the 300-600 km range. Note that the different correction curves are similar out to ca. 350 km that is the distance range where the majority of local events are recorded.

correction tables, the $q(r, f)$ -term in eq. (1.1), from the spreading and attenuation parameters in eq. (3.9). Such correction curves are shown in fig. 7 for the center frequencies and bandwidths of the bandpass filters used and the Alsaker *et al.* (1991) and NORSAR correction curves are included for comparison. In table II the ML_A magnitudes are very similar to the $ML(Ser)$ ones as expected from fig. 7 since the epi-

center distances seldom exceed 250 km. Likewise, the NORSAR reported M_L magnitudes are in average 0.3 units below the $ML(Ser)$ ones. This is also easily explained from fig. 7 since the NORSAR epicenter distances (see fig. 1) are mostly in the 300-600 km range where the associated correction curve is lower by ca. 0.3 units. In other words, our magnitude estimates and distance corrections pertain to epicenter dis-

tances well below 500 km. Ruud and Husebye (1992) have demonstrated that at least in Fennoscandia most of the station event recordings pertain to epicenter distances less than 500 km. If magnitude is to be retained as a standard earthquake size measure, a universal moment to magnitude formula may be constituted say by IASPEI, in order to avoid the prevailing confusion on type of event magnitude as published for local and regional events. A final remark is that near real time event magnitude estimates would be invaluable for estimating network monitoring capabilities also in near real time. Such estimates are tied to noise level estimates from the individual network stations in combination with a grid search procedure (e.g. Sereno and Bratt, 1989; Ringdal and Kværna, 1992). Another application now under consideration is to use near real time magnitude estimates as a part of automated epicenter location schemes (Ruud *et al.*, 1993; Sambridge and Gallager, 1993) that is by incorporating both phase and amplitude consistency in the phase association routine and hence in the final epicenter location.

6. Concluding remarks

In this study we have demonstrated that near real time magnitude estimation is feasible conditioned on a signal detector design for determining peak signal trace amplitudes. The results presented in table II imply that moment magnitudes are a viable alternative to conventional magnitude estimates. The advantages are an anchoring to seismic source theory and the use of clearly defined signal spreading and attenuation parameters. We have also demonstrated that the spreading and the attenuation parameters can be used for construction of correction tables commonly used in conventional magnitude determinations, thus avoiding tedious analysis of many earthquake recordings (Alsaker *et al.*, 1991).

Acknowledgements

Stimulating discussions with Bent Ole Ruud (Bergen University) and Dr. Anton Dainty (Philips Laboratory, Hanscom AFB, Ma) are hereby acknowledged. The research was supported by the Air Force Office of Scientific Research, USAF under Grant F49620-92-J-0510 (E.S.H.). TÜBITAK (Marmara Research Center) is thanked for providing the opportunity to participate in this work, while financial support from the Norwegian Research Council (NFR) is much appreciated (C.D.M.).

REFERENCES

AKI, K. (1967): Scaling law of seismic spectrums, *J. Geophys. Res.*, 73, 1217-1231.

ALSAKER, A., L.B. KVAMME, R.A. HANSEN, A. DAHLE and H. BUNGUM (1991): The M_L scale in Norway, *Bull. Seismol. Soc. Am.*, 81, 379-398.

BOORE, D.M. (1983): Stochastic simulation of high-frequency ground motions based on seismological models of the radiated spectra, *Bull. Seismol. Soc. Am.*, 73, 1865-1894.

BOORE, D.M. and W.B. JOYNER (1984): A note on the use of random vibration theory to predict peak amplitudes of transient signals, *Bull. Seismol. Soc. Am.*, 74, 2035-2039.

BÅTH, M. (1981): Local magnitude: recent research and current trends, *Earth Sci. Rev.*, 17, 315-398.

CARTWRIGHT, D.E. and M.S. LONGUET-HIGGINS (1956): The statistical distribution of the maxima of a random function, *Proc. Roy. Soc. London, Ser. A* 237, 212-223.

CRANDAL, S.H. and W.D. MARK (1963): Random Vibration in Mechanical Systems (Academic Press, New York and London).

DZIEWONSKI, A.M. and F. GILBERT (1974): Temporal variation of the seismic moment tensor and the evidence of precursive compression for two deep earthquakes, *Nature*, 247, 185-188.

EBEL, J.E. (1982): M_L measurements for Northeastern United States earthquakes, *Bull. Seismol. Soc. Am.*, 72, 1367-1378.

JOST, M.L. and R.B. HERRMANN (1989): A student's guide to and review of Moment Tensors, *Seismol. Res. Lett.*, 60 (2), 37-57.

NUTTLI, O.W. (1973): Seismic wave attenuation and magnitude relations for Eastern North America, *J. Geophys. Res.*, 78, 876-885.

RICHTER, C.F. (1935): An instrumental earthquake magnitude scale, *Bull. Seismol. Soc. Am.*, 25, 1-32.

RINGDAL, F. and T. KVÆRNA (1992): Continuous seismic threshold monitoring, *Geophys. J. Int.*, 111, 505-514.

RUUD, B.O. and E.S. HUSEBYE (1992): A new three-component detector and automatic single station bulletin production, *Bull. Seismol. Soc. Am.*, **82**, 221-237.

RUUD, B.O., C.D. LINDHOLM and E.S. HUSEBYE (1993): An exercise in automating seismic record analysis and network bulletin production, *Bull. Seismol. Soc. Am.*, **83**, 660-679.

SAMBRIDGE, M. and K. GALLAGHER (1993): Earthquake hypocenter location using genetic algorithms, *Bull. Seismol. Soc. Am.*, **83**, 1467-1491.

SERENO, T.J., S.R. BRATT and T.C. BACHE (1988): Simultaneous inversion of regional wave spectra for attenuation and seismic moment in Scandinavia, *J. Geophys. Res.*, **93**, 2019-2035.

SERENO, T.J. and S.R. BRATT (1989): Seismic detection capability at NORESS and implications for the detection threshold of a hypothetical network in the Soviet Union, *J. Geophys. Res.*, **94**, 10397-10414.

SINGH, S.K., M. ORDAZ, C.D. LINDHOLM and J. HAVSKOV (1990): Seismic hazard in Southern Norway, *Tech. Rep. Seismo-series N. 46*, University of Bergen, Norway.

XIE, J. (1993): Simultaneous inversion for source spectrum and path Q using L_8 with application to three semipalatinsk explosions, *Bull. Seismol. Soc. Am.*, **83**, 1547-1562.

Appendix

The relation between A_{rms} and $|A(f, r)|$:

Rayleigh's theorem gives the energy relation between the time and frequency domain representations such as:

$$\int_{-\infty}^{\infty} |a(t)|^2 dt = \int_{-\infty}^{\infty} |A(f)|^2 df \quad (A.1)$$

where $a(t)$ is the displacement in time and $|A(f)|$ is the amplitude spectrum. The unbiased rms estimate of the signal $a(t)$ in continuous time is defined as:

$$A_{rms}^2 = \frac{1}{\Delta T} \int_0^{\Delta T} |a(t)|^2 dt \quad (A.2)$$

where ΔT is window length in s. Likewise, for digital signals we have

$$A_{rms}^2 = \frac{1}{N} \sum_{i=0}^{N-1} a_i^2 \quad (A.3)$$

where N is the number of the samples. From eq. (3.1), we assume that $|A(f, r)|$ is flat within the pass-band of the filters used and this in combination with the Rayleigh's theorem leads to:

$$\begin{aligned} A_{rms}^2 &= \frac{1}{\Delta T} \int_{-f_B}^{f_B} |A(f)|^2 df \\ &= \frac{1}{\Delta T} \left[\int_{-f_2}^{-f_1} |A(f)|^2 df + \int_{f_1}^{f_2} |A(f)|^2 df \right] \\ &= \frac{1}{\Delta T} 2\Delta f |A(f_0)|^2 \end{aligned} \quad (A.4)$$

where f_B is the bandwidth of $a(t)$, f_1 and f_2 are the low and high cutoff frequencies of the bandpass filter, Δf is the filter bandwidth ($\Delta f = f_2 - f_1$) and f_0 is the center frequency [$f_0 = (f_1 + f_2)/2$] of the bandpass filter. Thus, eq. (A.4) gives us the relationship between the rms value of the signal $a(t)$ and the amplitude of the spectrum at the frequency f_0 which is expressed as:

$$|A(f_{0i}, r)| = \sqrt{\frac{\Delta T}{2\Delta f_i}} A_{\text{rms}}; \quad i = 1, \dots, 5 \quad (\text{A.5})$$

where f_{0i} and Δf_i are the center frequencies and the bandwidths of the 5 bandpass filters used in data analysis, $|A(f_{0i}, r)|$ is the amplitude spectrum of the displacement at epicentral distance r . In data analysis ΔT being the STA window length is fixed at 5 s independent of the bandpass filter used. In the context of detector design the STA window lengths seldom exceed a few seconds, however it is easy to combine short STA(rms) values in order to produce longer rms.

The relation between A_{max} and $|A(f, r)|$:

Assuming that the amplitude spectrum of the displacement $a(t)$ is flat within an idealized bandpass filtered trace, we have:

$$|A(f)| = A_0 \Pi_{\Delta f}(f - f_0) + A_0 \Pi_{\Delta f}(f + f_0) \quad (\text{A.6})$$

where $\Pi_{\Delta f}$ is a rectangular function with unit amplitude and bandwidth Δf , f_0 is the center frequency of $\Pi_{\Delta f}$ and A_0 is the amplitude of the displacement spectrum. If $A(f)$ is a real function, its inverse Fourier transform is:

$$a(t) = 2\Delta f A_0 \text{sinc}(\Delta f t) \cos(2\pi f_0 t) \quad (\text{A.7})$$

$a(t)$ has a maximum value at $t = 0$, namely

$$\begin{aligned} A_{\text{max}} &= 2\Delta f A_0 \\ &= 2\Delta f |A(f_{0i}, r)|; \quad i = 1, \dots, 5 \end{aligned} \quad (\text{A.8})$$

Eq. (A.7) is only valid in case of real functions (no phase shifts) which is hardly the case in seismology. However, since the *sinc* function varies rather slowly as compared to the *cos* function in eq. (A.7), it can be shown that the A_{max} relation in eq. (A.8) remains valid for practical purposes also for non-real functions.